J. Fluid Mech. (1990), *vol.* 210, *pp.* 23–55
Printed in Great Britain

Time-dependent and time-averaged turbulence structure near the nose of a wing–body junction

By WILLIAM J. DEVENPORT AND ROGER L. SIMPSON
Department of Aerospace and Ocean Engineering, Virginia Polytechnic Institute and State University, Blacksburg, VA 24061, USA

(Received 27 April 1988 and in revised form 3 May 1989)

The behaviour of a turbulent boundary layer on a flat surface as it encounters the nose of a cylindrical wing mounted normal to that surface is being investigated. A three-component laser anemometer has been developed to measure this highly turbulent three-dimensional flow. Measurements of all the non-zero mean-velocity and Reynolds-stress components have been made with this instrument in the plane of symmetry upstream of the wing. These data have been used to estimate some of the component terms of the turbulence kinetic energy equation. Histograms of velocity fluctuations and short-time cross-correlations between the laser anemometer and a hot-wire probe have also been measured in the plane of symmetry. In all, these results reveal much of the time-dependent and time-averaged turbulence structure of the flow here.

Separation occurs in the plane of symmetry because of the adverse pressure gradient imposed by the wing. In the time mean the resulting separated flow consists of two fairly distinct regions: a thin upstream region characterized by low mean backflow velocities and a relatively thick downstream region dominated by the intense recirculation of the mean junction vortex. In the upstream region the turbulence stresses develop in a manner qualitatively similar to those of a two-dimensional boundary layer separating in an adverse pressure gradient. In the vicinity of the junction vortex, though, the turbulence stresses are much greater and reach values many times larger than those normally observed in turbulent flows. These large stresses are associated with bimodal (double-peaked) histograms of velocity fluctuations produced by a velocity variation that is bistable. These observations are consistent with large-scale low-frequency unsteadiness of the instantaneous flow structure associated with the junction vortex. This unsteadiness seems to be produced by fluctuations in the momentum and vorticity of fluid from the outer part of the boundary layer which is recirculated as it impinges on the leading edge of the wing. Though we would expect these fluctuations to be produced by coherent structures in the boundary layer, frequencies of the large-scale unsteadiness are substantially lower than the passage frequency of such structures. It therefore seems that only a fraction of the turbulent structures are recirculated in this way.

1. Introduction

An appendage–body juncture flow is formed when a boundary layer on a surface encounters a protuberance or strut projecting from that surface. Upstream of the protuberance the time-averaged direction of the boundary-layer vorticity is spanwise across the surface. In order to satisfy the vortex theorems of fluid dynamics,

streamwise legs of this upstream vorticity stretch around the protuberance in a horseshoe shape with each leg having vorticity of the opposite sense. In most practical situations the protuberance has some aerofoil section and therefore imposes strong pressure gradients upon the junction flow. These greatly complicate the flow, producing a region of separation around the leading edge of the protuberance, a region of strong flow acceleration between the leading edge and maximum thickness, and a region of adverse pressure gradient (and possible separation) towards the trailing edge. This type of three-dimensional turbulent flow occurs in many situations of engineering interest, such as in turbomachinery blade and endwall flows, aircraft wing and body junction flows, and ship appendage and hull junction flows.

The flow in the immediate vicinity of the leading edge of such a protuberance is very poorly documented and understood. Surface oil-flow visualizations in this region have been performed for a variety of different appendage shapes (Belik 1973; Baker 1980; Rood 1984; Moore & Furlini 1984; Harsh 1985; Abid & Schmitt 1986; Dickinson 1986 and many others). These visualizations show complex and sometimes ambiguous patterns of oil streaks in the separated-flow region. Most workers have interpreted these patterns as showing the separation of the backflow upstream of the appendage and as a result find it necessary to speculate on the existence of multiple regions of recirculation in the mean flow away from the wall.

The structure of the instantaneous flow in the nose region has been observed by Falco (Van Dyke 1982, Plate 165) who studied the flow of a low-Reynolds-number turbulent boundary layer past an upright circular cylinder. His visualizations, performed using smoke, show that eddies in the outer region of the boundary layer are rapidly distorted as they approach the protuberance. He also reports seeing an intermittent rushing of fluid upstream from the leading edge of the protuberance in a 'jet' close to the wall.

Only Tree (1986) and Abid & Schmitt (1986) have made velocity measurements (using directionally sensitive laser anemometers) in the separated-flow region near the nose. Both of these studies used a wing with a circular leading edge. Tree mapped in great detail the mean-velocity field in the plane of symmetry but made no turbulence measurements. Abid & Schmitt present measurements of mean velocity and turbulence kinetic energy but their published results do not reveal the turbulence structure of the flow in much detail. Both of these studies show a simple region of intense recirculation adjacent to the wall in front of the protuberance, confined to an area less than one-fifth of the boundary-layer thickness in height.

The Reynolds-averaged effects of this junction vortex on the flow downstream of the nose, in the streamwise corner between the appendage and body, have been studied by a number of workers for several different appendage shapes (Shabaka & Bradshaw 1981; McMahon, Hubbart & Kubendran 1983; Mehta 1984; Moore & Furlini 1984; Rood 1984; Kubendran, McMahon & Hubbart 1986; Dickinson 1986). Despite the different appendages, all of these studies show the flow to have the same basic structure in this region. A strong secondary flow, associated with the junction vortex rotates so as to bring fluid close to the protuberance down towards the surrounding surface and then outwards across it. This action energizes the mean flow close to the surface. The junction vortex significantly alters the turbulence structure as well, enhancing turbulence levels near the centre of the secondary flow and suppressing them closer to the appendage. Effects on the turbulence shear stresses are also large, resulting in negative and non-isotropic eddy viscosities (Shabaka & Bradshaw 1981).

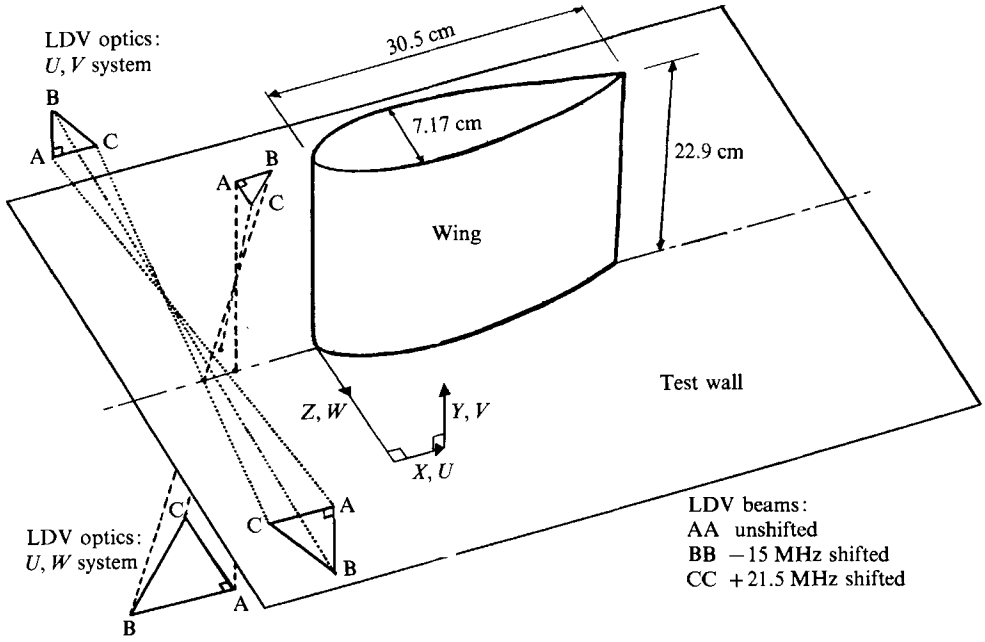

FIGURE 1. Perspective view of the wing–body junction showing the three-component LDV system.

Observations concerning the spectral characteristics of flows past appendage–body junctions have been made by Rood (1984) and Hasan, Casarella & Rood (1985). Rood's velocity measurements, on a cylindrical protuberance with a 3:2 semi-elliptic nose, show extensive spatial coherence in the vortex flow downstream of the protuberance at low frequencies. Frequencies in one bandwidth $f\delta/U_\infty = 0.04$ to 0.13, where δ and U_∞ are the thickness and edge velocity of the undisturbed approach boundary layer, appear to emanate from the nose region of the junction. The wall-pressure spectra of Hasan *et al.*, for a similar configuration with a 3:1 elliptical nose, show pressure fluctuations in the separated flow ahead of the protuberance to be most intense for $f\delta/U_\infty$ between about 0.008 and 0.08. In the corner flow accelerating between the nose and maximum thickness there is some suggestion of a second frequency band between $f\delta/U_\infty$ of about 0.07–0.17.

The purpose of our continuing investigation is to study in detail the time-averaged and time-dependent properties of the flow past an idealized wing–body junction. In this paper we shall present detailed laser-anemometer measurements made in the region of separated flow immediately upstream of the leading edge of the wing.

2. Experimental apparatus and instrumentation

2.1. *The wing*

The wing (figure 1) is cylindrical. Its cross-section consists of a 3:2 elliptical nose (with its major axis aligned with the chord) and NACA 0020 tail joined at the maximum thickness. It has a maximum thickness of 7.17 cm, a chord of 30.5 cm and a height of 22.9 cm.

The boundary layer on the wing is tripped to avoid any unsteadiness or uneveness in the flow that may result from natural transition. Trip wires of circular cross-

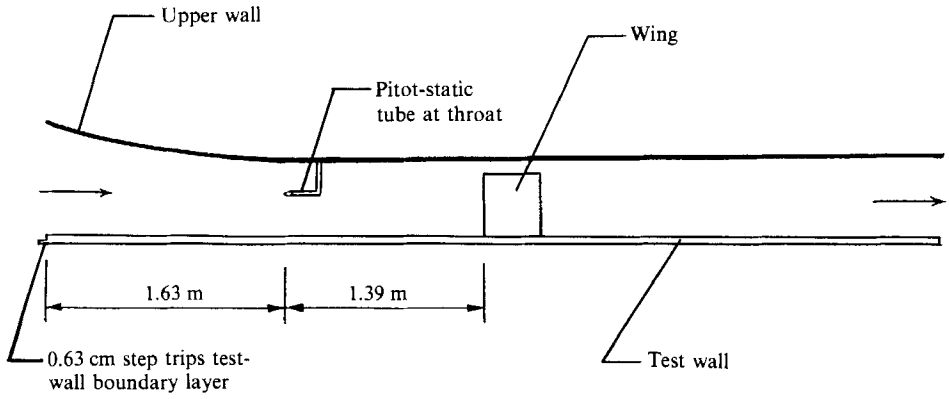

FIGURE 2. Side-view schematic of the wind-tunnel test section for the wing–body junction experiments. Vertical scale exaggerated to show detail.

section, 1 mm in diameter, are attached 10 mm upstream of the maximum thickness of the wing. This diameter was chosen according to criteria stated by Schlichting (1968) to ensure that the wires would be fully effective at the lowest flow speeds of interest.

2.2. *The wind tunnel*

The wind tunnel is of an open-circuit type and is powered by a centrifugal blower. Air from the blower is supplied to a test section after first passing through a fixed-setting damper, a plenum, a section of honeycomb to remove the mean swirl of the flow, seven screens to remove much of the turbulence intensity, and a 4:1 contraction to further reduce turbulence levels and accelerate the flow to test speed. The potential core of the flow entering the test section is uniform to within 0.5% in the spanwise direction and 1% in the vertical direction and has a turbulence intensity of 0.2% at 27 m/s. This tunnel has been used in much previous research at VPI & SU and at Southern Methodist University.

The wind-tunnel test section (figure 2) is 6 m long, 0.91 m wide and has a rectangular cross-section. Flow entering the test section is subjected to a further 1.5:1 contraction produced by the shape of the upper wall. A throat is reached 1.63 m downstream of the entrance where the test section is 25.5 cm in height. Downstream of the throat the upper wall is almost parallel to the (flat) lower test wall, diverging gradually from it with distance downstream. In the absence of the wing this arrangement produces a flow of very nearly zero streamwise pressure gradient and thus an equilibrium boundary layer on the test wall. This boundary layer, which is tripped by a 0.63 cm high step at the test-section entrance, was studied during the first part of this research (Ahn 1986; Devenport & Simpson 1986). This work shows its statistical and spectral properties to be very much like those of equilibrium boundary layers studied by previous workers. Measurements made in the boundary layer closely satisfy the two-dimensional momentum integral equation. Velocity and pressure spectra show no preferred frequencies.

The wing was mounted on the test wall at zero incidence and sweep with its leading edge 1.39 m downstream of the throat. As recommended by Dechow (see Dechow & Felsch (1977)) a gap (of 37 mm) was left between the upper end of the wing and the upper wall of the wind tunnel. This gap prevented the formation of a second junction

vortex here which might have interfered with the flow on the test wall further downstream. Inserts for the wind-tunnel sidewalls were constructed to minimize blockage-induced pressure gradients around the wing.

2.3. *Laser Doppler anemometer*

A three-component laser Doppler velocimeter (LDV) was used to measure the magnitude and direction of the mean-velocity vector, elements of the Reynolds-stress tensor and other properties of the flow.

The LDV uses a Coherent Innova 90 argon–ion laser operated at a wavelength of 514.5 nm with a power of about 1.5 W. Light from the laser is passed through a dual Bragg cell containing 21.5 MHz and 15 MHz transducers. The Bragg cell is adjusted so that almost all the light leaving it is in four beams of approximately equal intensity, one unshifted and the other three shifted by -15, 21.5 and 6.5 MHz. One of three different sets of sending optics is used to direct these beams to the measurement volume. Each set of sending optics produces an arrangement of the beams that is sensitive to a different pair of velocity components. Only one set of sending optics is used at any one time.

The optical system designed by Simpson & Chew (1979) is used to measure velocity components in the (U, V)-plane. This system produces three convergent beams (unshifted, $+21.5$ MHz shifted and -15 MHz shifted) that enter the wind tunnel through one of its glass sidewalls, as shown in figure 1. In the measurement volume these beams produce moving fringe patterns sensitive to U-, V- and $(U-V)$-component velocities, with small contributions from W that were negligible in the present experiments. The U, W optical system (figure 1) produces a similar arrangement of these three beams which in this case enter the wind tunnel through a Plexiglas plate set in the test wall. At their crossing point these beams produce moving fringe patterns sensitive to U-, W- and $(U-W)$-component velocities with negligible contributions from V. The V, W optical system, which was not used for measurements presented here, is described by Devenport & Simpson (1987).

The flow is seeded using a dioctal phthalate smoke produced by the aerosol generator described by Simpson & Chew (1979), originally designed by Echols & Young (1963). Smoke is injected into the test-wall boundary layer through a slot located at the step where this boundary layer is tripped (see figure 2). Since the smoke is ultimately discharged into the laboratory some of it returns through the centrifugal blower providing seeding particles in the free stream.

Light scattered from the measurement volume is collected through the sidewall of the wind tunnel, about 20° away from the axis of the U, V optics in the downstream direction. The scattered light is focused on to the 200 μm pinhole of a single photomultiplier tube by a large converging lens. This off-axis scattering arrangement makes the effective size of the U, V and U, W measurement volumes $0.3 \times 0.3 \times 0.6$ mm and $0.07 \times 0.3 \times 0.07$ mm in the X-, Y- and Z-directions respectively.

Reynolds-averaged velocity measurements are obtained from the photomultiplier signal using the technique known as fast-sweep-rate sampling spectrum analysis. This method, described in detail by Simpson & Barr (1974, 1975) and Simpson & Chew (1979) involves the detection of peaks in the output of a rapidly swept filter spectrum analyser. When using this method, only a fraction of those particles traversing the measurement volume are detected (about 400 to 500 per s). This means that data obtained from different signals over the same period of time will not have been produced by the same set of seeding particles. The Reynolds shear stresses

	Near-wall region	Backflow	Vortex centre	Outer region
$\overline{U}/U_{\mathrm{ref}}$	0.07	−0.34	0.06	0.56
$\overline{u^2}/U_{\mathrm{ref}}^2$	0.014	0.052	0.041	0.003
$-\overline{uv}/U_{\mathrm{ref}}^2$	0.0001	0.0070	0.0065	0.0002
$\delta(\overline{U}/U_{\mathrm{ref}})$	0.025	0.025	0.025	0.025
$\delta(\overline{u^2}/U_{\mathrm{ref}}^2)$	0.0005	0.0016	0.0013	0.0001
$\delta(-(uv)/U_{\mathrm{ref}}^2)$	0.0003	0.0013	0.0019	0.0001
$\delta(-T/U_{\mathrm{ref}}^3\, 2\overline{u^2}\,\partial U/\partial X)$	0.016	0.120	0.086	0.004
$\delta(-T/U_{\mathrm{ref}}^3\, 2\overline{v^2}\,\partial V/\partial Y)$	0.002	0.022	0.039	0.00003
$\delta(-T/U_{\mathrm{ref}}^3\, 2\overline{v^2}\,\partial W/\partial Z)$	0.011	0.029	0.034	0.0008
$\delta(-T/U_{\mathrm{ref}}^3\, 2\overline{uv}\,\partial U/\partial Y)$	0.011	0.084	0.061	0.0001
$\delta(-T/U_{\mathrm{ref}}^3\, 2\overline{uv}\,\partial V/\partial X)$	0.00005	0.004	0.014	0.0001
δ (total production)	0.016	0.120	0.082	0.004
$\delta(-T/U_{\mathrm{ref}}^3\, U\partial\overline{u^2}/\partial X)$	0.003	0.067	0.003	0.0019
$\delta(-T/U_{\mathrm{ref}}^3\, U\partial\overline{v^2}/\partial X)$	0.0007	0.033	0.006	0.001
$\delta(-T/U_{\mathrm{ref}}^3\, U\partial\overline{w^2}/\partial X)$	0.0012	0.012	0.004	0.0009
$\delta(-T/U_{\mathrm{ref}}^3\, V\partial\overline{u^2}/\partial Y)$	0.003	0.010	0.002	0.0001
$\delta(-T/U_{\mathrm{ref}}^3\, V\partial\overline{v^2}/\partial Y)$	0.0005	0.005	0.002	0.00007
$\delta(-T/U_{\mathrm{ref}}^3\, V\partial\overline{w^2}/\partial Y)$	0.0013	0.003	0.0006	0.00006
δ (total advection)	0.005	0.076	0.007	0.0024

TABLE 1. Estimates of 95% confidence limits (δ) for measurements made with the LDV

therefore cannot be obtained directly by multiplying the signals of different velocity components. Instead they are obtained using the mean square of signals that correspond to the difference of velocity components.

The small diameter of the U, W measurement volume caused some finite-transit-time broadening of the corresponding signals. This error results from having only a small number of fringes in the measurement volume. It increases the measured turbulence intensity by an amount in proportion to the mean velocity while leaving the mean velocity unaffected. It is therefore simple to correct. Corrections obtained using the theory described by Durst, Melling & Whitelaw (1981) have been applied where necessary to the data presented in this paper.

Uncertainty estimates for the LDV measurements are listed in table 1. It should be mentioned that turbulence measurements in the free stream are not reliable because of the lack of seeding particles here and inaccuracies in the corrections for finite-transit-time broadening.

3. Results and discussion

Results will be presented using the right-handed coordinate system (X, Y, Z) and (U, V, W) defined in figure 1. Distances are non-dimensionalized by the maximum thickness of the wing T, equal to 71.7 mm. Velocities are non-dimensionalized by U_{ref}, the approach main-stream velocity measured using a Pitot-static tube mounted in the wind-tunnel throat 1.39 m upstream of the nose of the wing. Under nominal test conditions the momentum-thickness Reynolds number of the approach boundary layer, measured $2.15T$ upstream of the wing leading edge, was 6700, corresponding to a total boundary-layer thickness $\delta_{99.5}$ of 36 mm ($\delta_{99.5}/T = 0.50$) and U_{ref} of 27 m/s.

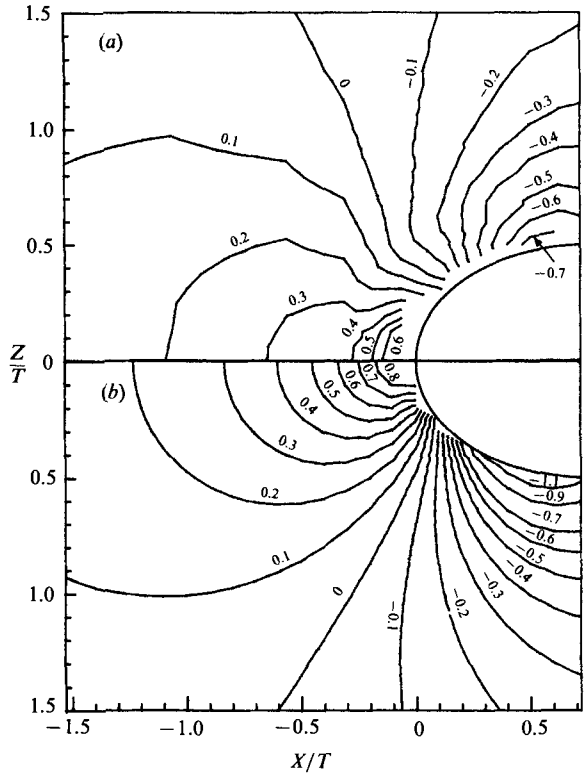

FIGURE 3. Contours of mean pressure coefficient in the vicinity of the nose of the wing, (*a*) measured on test wall, (*b*) calculated for free stream.

3.1. *Surface-pressure measurements and oil-flow visualization*

Figure 3 shows contours of mean static pressure coefficient C_p measured on the test wall in the vicinity of the nose of the wing. Contours for the free stream calculated by assuming two-dimensional unbounded potential flow are also drawn. C_p, defined as $(p-p_{\mathrm{ref}})/(p_0-p_{\mathrm{ref}})$, where p_0 and p_{ref} are the stagnation and static pressures of the undisturbed free stream, has an uncertainty of about 0.006 for the measurements. However, the difficulty of assigning exactly equivalent reference pressures for the measurement and calculation means that there is an additional uncertainty in their comparison of about 0.02 in C_p.

The wall and free-stream pressure distributions are qualitatively fairly similar despite the fact that the magnitude of the wall C_p is considerably lower in the immediate vicinity of the wing because of the boundary layer. An interesting feature seen only on the wall is the distortion of the measured contours that occurs about $0.3T$ from the wing surface. This is probably due to the lowering of the pressure in the vicinity of the junction vortex. Measurements (not plotted in figure 3) show the pressure distribution about the wing to be very closely symmetrical.

Figure 4 shows a surface oil-flow visualization performed on the test wall around the wing nose. A line of separation, wrapped around the wing, originates at a saddle (or separation) point in the plane of symmetry $0.47T$ upstream of the wing leading edge. (Strictly speaking, a line of attachment, coincident with the plane of symmetry, also passes through this saddle point.) Separation occurs because of the

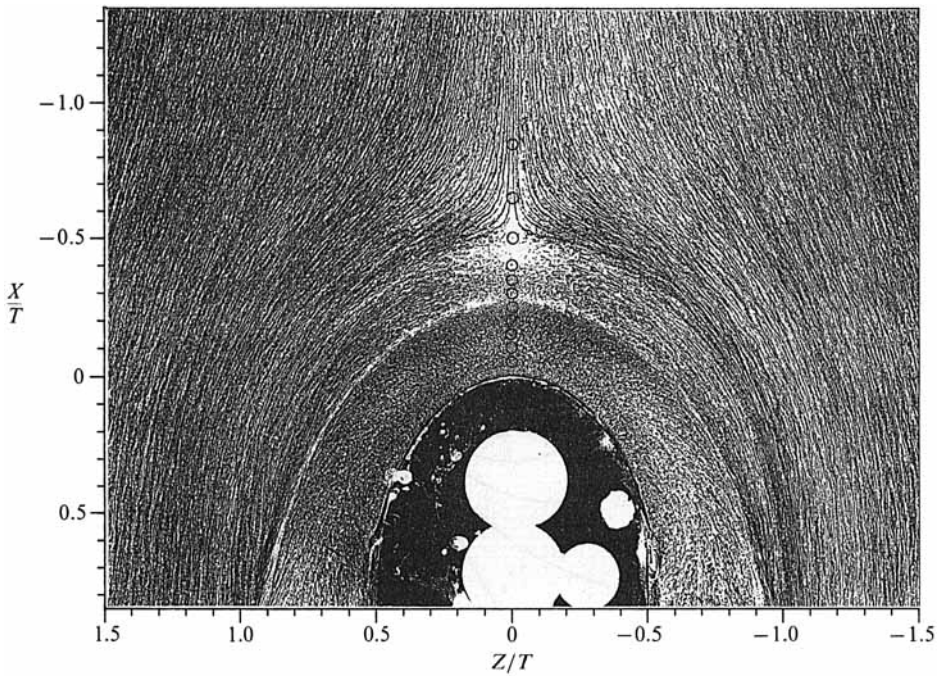

FIGURE 4. Surface oil-flow visualization performed on the test wall surrounding the wing nose. Circles show locations of LDV measurements in the plane of symmetry.

strong adverse pressure gradient imposed by the wing in this region (figure 3). Surprisingly, away from the saddle point, the separation line is not initially marked by much accumulation of pigment. Instead pigment has built up on a line formed closer to the wing that crosses the plane of symmetry $0.28T$ upstream of the wing. Close to the plane of symmetry this line is not a separation or reattachment since the oil streaks here pass through it. Measurements made by Devenport & Simpson (1989) show this to be a line of low streamwise shear. This line divides the separated flow into two distinct regions: a strip of high surface shear stresses adjacent to the wing, presumably generated by the time-averaged action of the horseshoe vortex, and a crescent-shaped region of apparently lower shear stresses upstream. Although not clearly visible in figure 4, oil-flow visualizations did show the presence of a small region of secondary separation in the corner between the wall and wing. This was observed as a reattachment line on the wall and a line of separation on the wing about $0.025T$ from the corner in the plane of symmetry.

3.2. *Reynolds-averaged measurements of velocity*

Measurements were made using the laser anemometer at a number of the stations in the plane of symmetry (figure 4). Uncertainties in these data are listed in table 1.

Mean-velocity measurements, drawn as vectors in figure 5, show the expected presence of the time-mean junction vortex. This roughly elliptical structure, centred near $X/T = -0.2$, $Y/T = 0.05$ generates an intense backflow by reversing fluid impinging on the leading edge of the wing. The backflow reaches a maximum mean velocity of $0.48U_{\text{ref}}$ and then decelerates, giving the appearance of reseparation between $X/T = -0.25$ and -0.3 in the vicinity of the line of low shear. Reseparation, however, does not occur, as a thin region of weak reversed flow is sustained adjacent

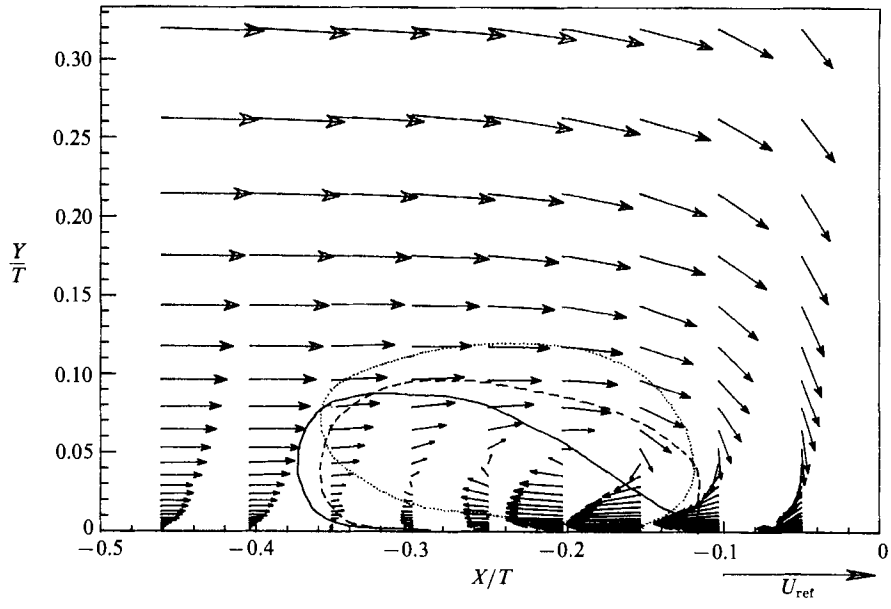

FIGURE 5. Time-mean velocity vectors in the plane of symmetry. Solid, dashed and dotted lines show bimodal regions for the U-, V- and $(U-V)$-component velocity histograms respectively.

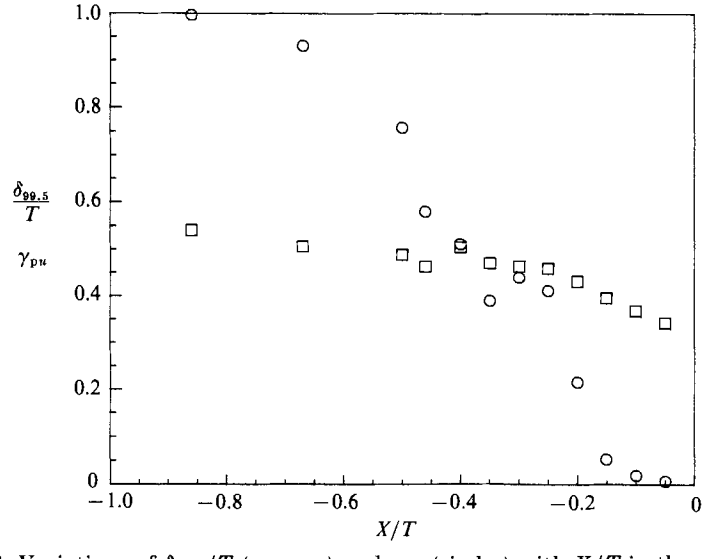

FIGURE 6. Variations of $\delta_{99.5}/T$ (squares) and γ_{pu} (circles) with X/T in the plane of symmetry.

to the wall. This region is then all that persists of the backflow upstream to the separation point at $X/T = -0.47$.

The near-wall behaviour of the separated flow is illustrated to a certain extent in figure 6. This shows the variation of γ_{pu}, the fraction of time for which the flow is in the positive U-direction, in the plane of symmetry as deduced from laser-anemometer measurements made 0.01 in. ($0.003T$) from the wall. Figure 6 shows the expected *fall* in γ_{pu} as the flow approaches separation at $X/T = -0.47$ (γ_{pu} should pass through 0.5 near a separation point). Between separation and the line of low shear γ_{pu}

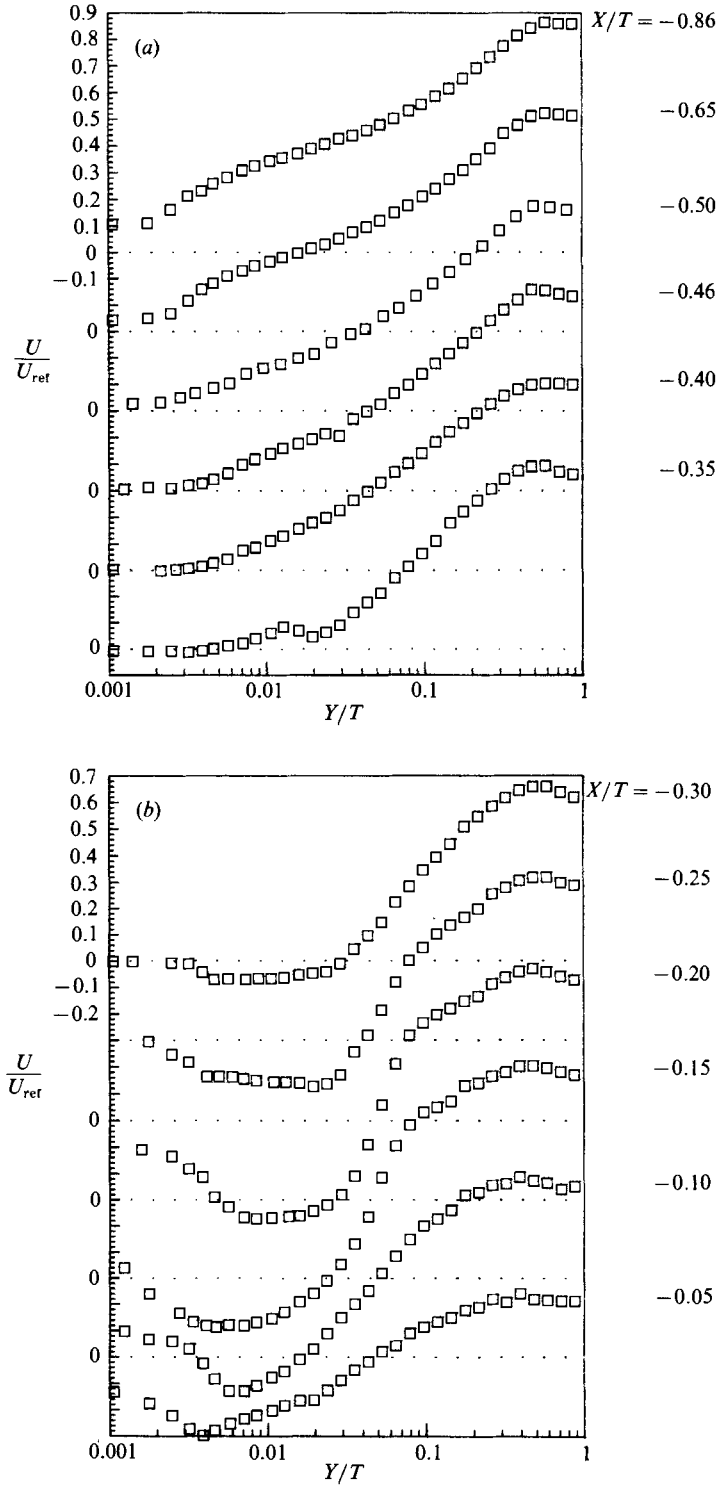

FIGURE 7(*a*, *b*). Profiles of time-mean velocity U/U_{ref}.

remains approximately constant at around 0.45. The implication is that instantaneously this zone is one of intermittent forward and reverse flow and not one of organized detachment. Closer to the wing, under the influence of the junction vortex, γ_{pu} falls, becoming almost zero at $X/T = -0.1$ and -0.05.

The flow approaching the nose of the wing is subjected to the strong adverse pressure gradient illustrated in figure 3. On either side of the plane of symmetry, cross-stream pressure gradients, which steepen as the wing is approached, tend to draw flow away from the plane of symmetry in the spanwise direction. The effects of this pressure field and of the junction vortex can be seen in the profiles of mean velocity, turbulent stresses and correlation coefficients plotted on semilogarithmic scales in figures 7–10.

From the most upstream station ($X/T = -0.86$) to the vicinity of the separation point ($X/T = -0.46$) these measurements reveal a flow developing in a manner not unlike a two-dimensional turbulent boundary layer in an adverse pressure gradient (see for example Simpson, Chew & Shivaprasad 1980, 1981; Shiloh, Shivaprasad & Simpson 1981). The outer region of the mean-velocity profile grows here, engulfing the log-law region (figure 7*a*). The peak levels of the turbulence stresses increase, the peak in $\overline{u^2}$ moving away from the wall (figure 9*a*). Over the outer part of the boundary layer $\overline{v^2}$ and $\overline{w^2}$ are approximately equal and the ratios $(\overline{v^2}/\overline{u^2})^{\frac{1}{2}}$ and $(\overline{w^2}/\overline{u^2})^{\frac{1}{2}}$ remain approximately constant between about 0.5 and 0.6. The two correlation coefficients $-\overline{uv}/(\overline{u^2}\overline{v^2})^{\frac{1}{2}}$ and $-\overline{uv}/(\overline{u^2}+\overline{v^2}+\overline{w^2})$ remain fairly constant over most of the boundary layer, at about 0.35 and 0.1 respectively (figure 10) and vary little with distance downstream. (Note that the erratic variations of the coefficients in the near-wall region are thought to be due to uncertainty in the measurement of $-\overline{uv}$ and are not physically significant.)

However, this two-dimensional analogy is limited. The boundary-layer thickness in this region (plotted in figure 6) falls with distance downstream instead of increasing, as would normally be expected in an adverse pressure gradient. A comparison between the profiles of $\overline{u^2}/U_{\text{ref}}^2$ and $-\overline{uv}/U_{\text{ref}}^2$ at $X/T = -0.5$, 0.8δ upstream of separation, and those of Simpson *et al.* (1980), 0.25δ upstream of separation in a two-dimensional boundary layer, shows that the peaks of the present profiles are much closer to the wall (figures 8*a* and 9*a*). These three-dimensional effects are due, at least in part, to the removal of fluid from the plane of symmetry by the cross-stream pressure gradients acting on either side. These gradients affect most the low-momentum boundary-layer fluid close to the wall and thus act to reduce the boundary-layer thickness and hold the boundary layer to the wall.

An interesting three-dimensional effect with no obvious explanation is apparent in the near-wall behaviour of the turbulent normal stress $\overline{w^2}$ in this zone (figure 9*a*). As the wall is approached $\overline{w^2}$ remains approximately constant at its peak value becoming equal to, if not exceeding, $\overline{u^2}$ very close to the wall. In two-dimensional boundary layers $\overline{w^2}$ remains a small fraction of $\overline{u^2}$ as the wall is neared (Shiloh *et al.* 1981; Sandborn & Slogar 1955; Schubauer & Klebanoff 1950).

Between separation and the line of low shear ($-0.47 < X/T < -0.28$) the mean-velocity profiles (figure 7*a*, *b*) develop maxima near the boundary-layer edge. The continuing reduction of boundary-layer thickness in this region (figure 6) indicates a curvature of the free stream sufficient to account for this. In the thin region of mean backflow that occupies most of this region (figure 5) the mean-velocity gradient at the wall remains very small (figures 7*a*, *b*), consistent with the oil-flow visualization (figure 4) and the variation of γ_{pu} (figure 6). Upstream of $X/T = -0.3$, where some

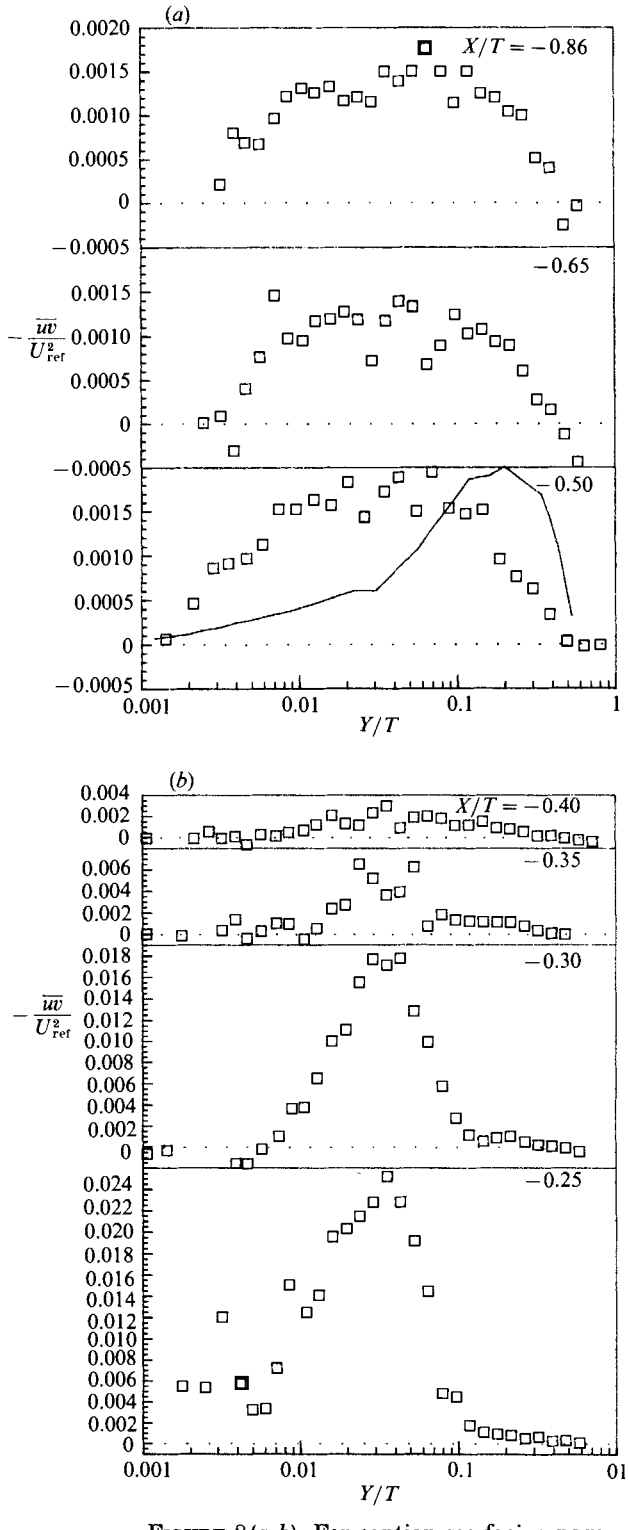

FIGURE 8(*a*,*b*). For caption see facing page.

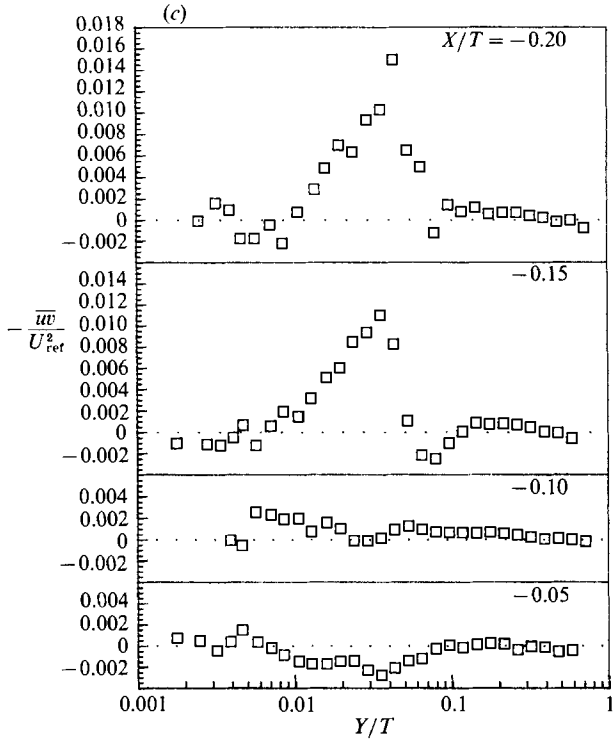

FIGURE 8(*a–c*). Profiles of the turbulent shear stress $-\overline{uv}/U_{ref}^2$. Solid line shows $-\overline{uv}$ data of Simpson *et al.* (1980) for a two-dimensional boundary layer separating in an adverse pressure gradient. (These data are compared by scaling them on the local boundary-layer thickness and edge velocity.)

of the reversed flow is associated with the mean junction vortex, the weak backflow is probably generated by the turbulent structures of the boundary layer as they decelerate in the adverse pressure gradient. The low momentum of this reversed fluid makes it especially susceptible to the cross-stream pressure gradients on either side of the plane of symmetry, perhaps explaining why this region remains so thin. As will become clear the kinks in the mean velocity profiles at $X/T = -0.35$ and -0.3 are associated with unsteady motion in the vicinity of the junction vortex.

The turbulent stresses measured in this zone show the effects of separation and, at $X/T = -0.35$ and -0.3, the increasing influence of the junction vortex. The profiles of $-\overline{uv}/U_{ref}^2$ and $\overline{v^2}/U_{ref}^2$ develop pronounced peaks between $Y/T = 0.01$ and 0.1 that appear symmetrical on the semilogarithmic scales of figures 8(*b*) and 9(*b*). The corresponding profiles of $\overline{u^2}/U_{ref}^2$ develop in a similar way except that they also show substantial increases in the turbulence level between $Y/T = 0.004$ and 0.01. $\overline{w^2}/U_{ref}^2$ increases little in this zone as do all the stresses in the outer part of the boundary layer ($X/T > 0.1$).

Under the immediate influence of the junction vortex, between $X/T = -0.3$ and -0.15, the profiles of mean and turbulence quantities cease to bear much resemblance to those of a boundary layer in an adverse pressure gradient. The circulation of the mean vortex dominates the mean-velocity profiles (figure 7*b*). The maxima in the outer part of these profiles, attributed to curvature of the free stream, persists, moving slightly towards the wall as the wing is approached. Within the

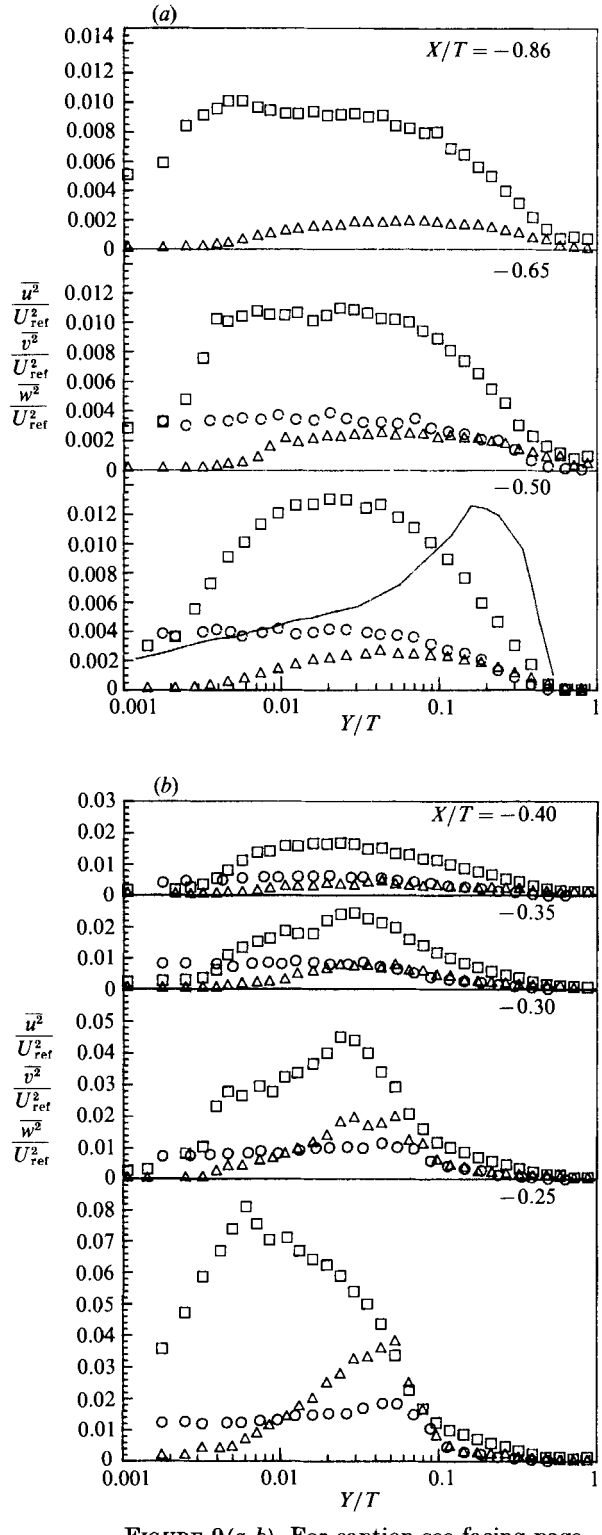

FIGURE 9(a, b). For caption see facing page.

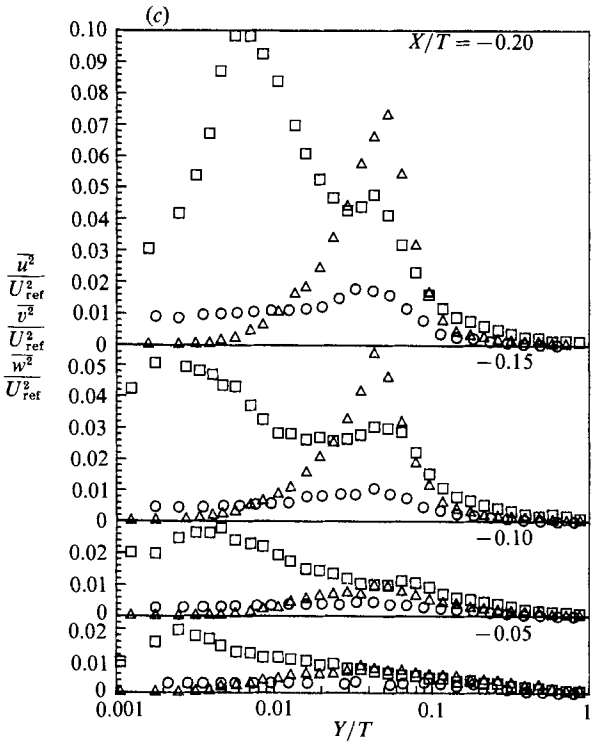

FIGURE 9(*a–c*). Profiles of the turbulent normal stresses $\overline{u^2}/U_{ref}^2$ (squares), $\overline{v^2}/U_{ref}^2$ (triangles) and $\overline{w^2}/U_{ref}^2$ (circles). Solid line shows $\overline{u^2}$ data of Simpson *et al.* (1980) for a two-dimensional boundary layer separating in an adverse pressure gradient. (These data are compared by scaling them on the local boundary-layer thickness and edge velocity.)

time-mean vortex the turbulence stresses are very large. The maximum recorded values of $-\overline{uv}/U_{ref}^2$, $\overline{v^2}/U_{ref}^2$ and $\overline{w^2}/U_{ref}^2$ are all reached about $0.04T$ from the wall in the area of high mean-velocity gradient near the centre of the vortex. This fact alone, though, does not seem to be enough to explain the sizes of these stresses which at some locations are more than an order of magnitude greater than those normally observed in turbulent boundary layers. $\overline{v^2}/U_{ref}^2$ becomes particularly big, reaching a maximum of 0.073 (0.225 if non-dimensionalized by the local edge velocity) at $X/T = -0.2$. Large values of $\overline{u^2}/U_{ref}^2$ were also recorded close to the centre of the mean vortex. However, this stress reaches its maximum recorded value of $0.098U_{ref}^2$ much closer to the wall, near $Y/T = 0.006$, where both $\overline{v^2}$ and $\overline{w^2}$ are comparatively small. The high turbulence stresses near the centre of the mean junction vortex are associated with increased values of the correlation coefficients $-\overline{uv}/(\overline{u^2v^2})^{\frac{1}{2}}$ and $-\overline{uv}/(\overline{u^2}+\overline{v^2}+\overline{w^2})$ of about 0.55 and 0.2. Results presented and discussed below show this to be a result of large-scale coherence in the instantaneous flow here.

Above the junction vortex ($Y/T > 0.2$) the turbulence stresses fall with distance downstream, perhaps as a result of the distortion and stretching of turbulent structures in the imposed pressure field. The appearance of negative Reynolds shear stresses close to $Y/T = 0.08$ at $X/T = -0.15$ may be a result of the angle of the flow here with respect to our laboratory fixed coordinate system.

Downstream of the centre of the mean junction vortex ($X/T = -0.1$ and -0.5) the normal turbulence stresses, at all positions in the profiles, decrease rapidly with X,

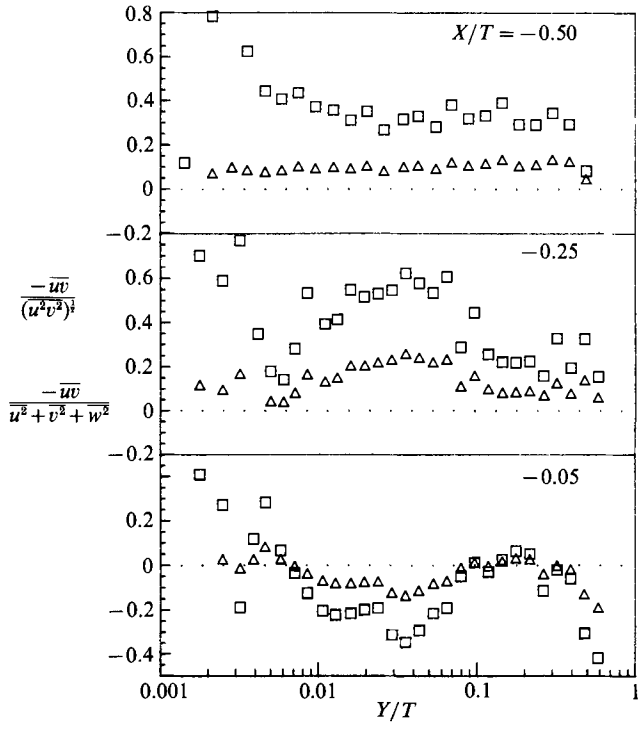

FIGURE 10. Selected profiles of the correlation coefficients $-\overline{uv}/(\overline{u^2}\,\overline{v^2})^{\frac{1}{2}}$ (squares) and $-\overline{uv}/(\overline{u^2}+\overline{v^2}+\overline{w^2})$ (triangles).

reaching comparatively small values immediately upstream of the wing. The Reynolds shear stress also decreases, becoming negative over much of the boundary layer at $X/T = -0.05$. These effects are presumably a result of turbulent fluctuations being inhibited by the wing and of the gross distortion of the instantaneous boundary-layer structure that must be present in this region. Extrapolation of figure 6 suggests a time-averaged boundary-layer thickness of $0.3T$ at the wing leading edge, 60% of its initial value.

3.3. *Probability-density functions of velocity*

Conventional turbulent mixing does not seem sufficient to explain the very large turbulence stresses recorded in the vicinity of the mean junction vortex. These stresses are, however, associated with unusual histograms of velocity probability-density functions (p.d.f.s) that suggest the presence of another mechanism.

Figure 11 shows a series of p.d.f.s of U measured during the traverse performed at $X/T = -0.2$ through the centre of the mean vortex. Above the mid-height of the vortex, $Y/T > 0.05$, the p.d.f.s have the approximately Gaussian form typical of turbulent flows. Below $Y/T = 0.05$ the distributions are bimodal, appearing as though they have been produced by the addition of two roughly Gaussian distributions, or 'peaks', with different mean values. U-component histograms of this type were observed at other streamwise locations as well, within the region indicated by the line drawn in figure 5. Bimodal p.d.f.s were also observed in the V- and $(U-V)$-components but over slightly different regions (figure 5). This phenomenon is absent from the W-component.

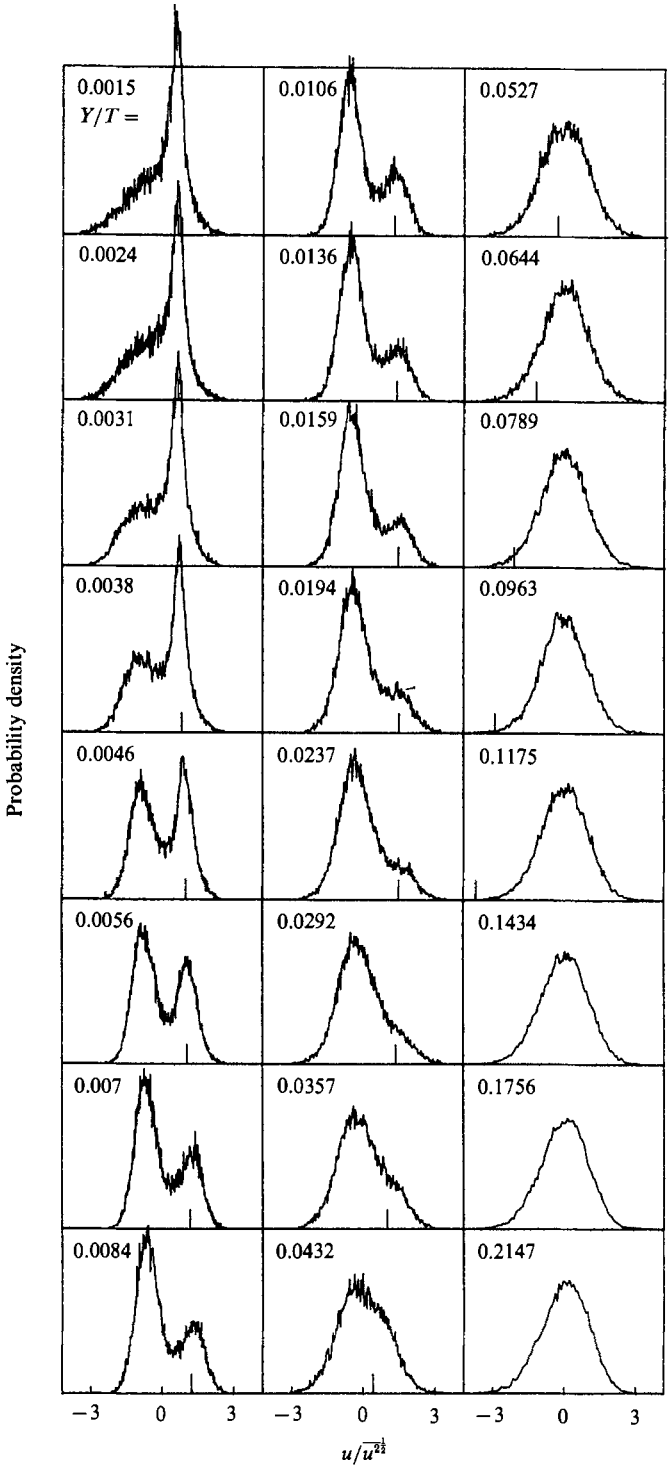

FIGURE 11. Probability-density functions of U-component velocity fluctuations at $X/T = -0.20$. Ticks on abscissae indicate zero U.

As is obvious from figure 11, the bimodal p.d.f.s do not all have the same shape – the relative size and separation of the two peaks comprising each p.d.f. varying with position, the variance (the turbulence normal stress) changing accordingly. The maxima of $\overline{u^2}$, $\overline{v^2}$ and $\overline{(u-v)^2}$ all occur close to the point where the two peaks of the corresponding p.d.f. are furthest apart. An interesting feature of the U-p.d.f.s is that, despite these changes in shape, one peak is almost always centred near zero velocity and the other at large negative velocity.

Since at a point the U-, V- $(U-V)$- and W-p.d.f.s represent projections of the same joint velocity probability-density function, this joint p.d.f. must be bimodal throughout the aggregate of the regions drawn in figure 5. The existence of the joint p.d.f. requires the ratio between the areas of the two peaks of a bimodal histogram to be the same for all velocity components at a point, whether or not the peaks can be distinguished in every component. Thus, the absence of bimodal histograms in the W-component means that the two peaks of the joint p.d.f. are always centred on the same value of W (zero). The bimodal regions of U, V and $U-V$ are not exactly coincident for the same reason.

Double-peaked histograms of velocity fluctuations imply that the velocity has two preferred states. With reference to the U-p.d.f.s (most of which have a peak at large negative velocity and one at near zero velocity) we shall call these two states the backflow mode and the zero-flow mode. The peaks in the V-p.d.f.s associated with the zero- and backflow modes may be identified by requiring that the ratio of the area of those peaks to the area of the entire p.d.f. be approximately the same as in the U-p.d.f.s.

An approximate method has been devised to obtain from each bimodal histogram estimates of the average velocities associated with the zero- and backflow modes and an estimate of the proportion of time γ_b for which the backflow mode is present. The method assumes that the larger peak of each bimodal histogram is symmetrical, with a shape determined by its unattached side. This symmetrical distribution is then subtracted from the original histogram to yield an estimate of the shape of the other peak. The average velocities associated with the two modes may then be calculated. γ_b is given by the ratio of the area of the peak associated with the backflow mode to that of the original histogram. This procedure provides reasonably consistent data throughout most of the bimodal region. However, at locations where there are large differences between the size of the peaks or the peaks are close together, uncertainties in the calculated velocities are substantial and γ_b cannot be reliably estimated.

Since both U- and V-component histograms were analysed in this fashion velocity vectors associated with the backflow mode (figure 12) and with the zero-flow mode (figure 13) may be drawn. Note that the regular mean-velocity vectors have been plotted in these figures at locations where the separate modes could not easily be distinguished (i.e. towards the edges of, and outside, the bimodal region).

To appreciate the physical significance of these vector fields it is necessary to examine the distribution of γ_b in the bimodal region, plotted as contours in figure 14. Note that these contours are only drawn where γ_b could be confidently estimated.

Near the downstream edge of the bimodal region γ_b approaches 1, implying that the flow here is almost always in the backflow mode. γ_b decreases monotonically with distance upstream falling to near zero at the upstream edge of the bimodal region, the zero-flow mode dominating here. The flow in the bimodal region is thus normally a combination of the zero- and backflow modes so figures 12 and 13 can at best only represent extreme and comparatively rare states of the flow. Intermediate states may be better represented by combinations of these two plots. If we assume that the

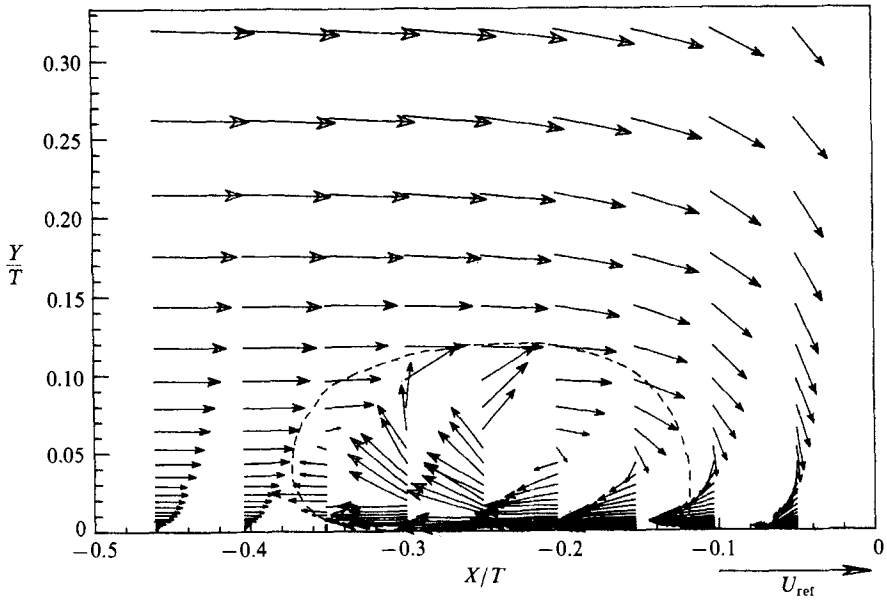

FIGURE 12. Velocity vectors of the backflow mode (dotted line shows the extent of the aggregate of the bimodal regions of figure 5).

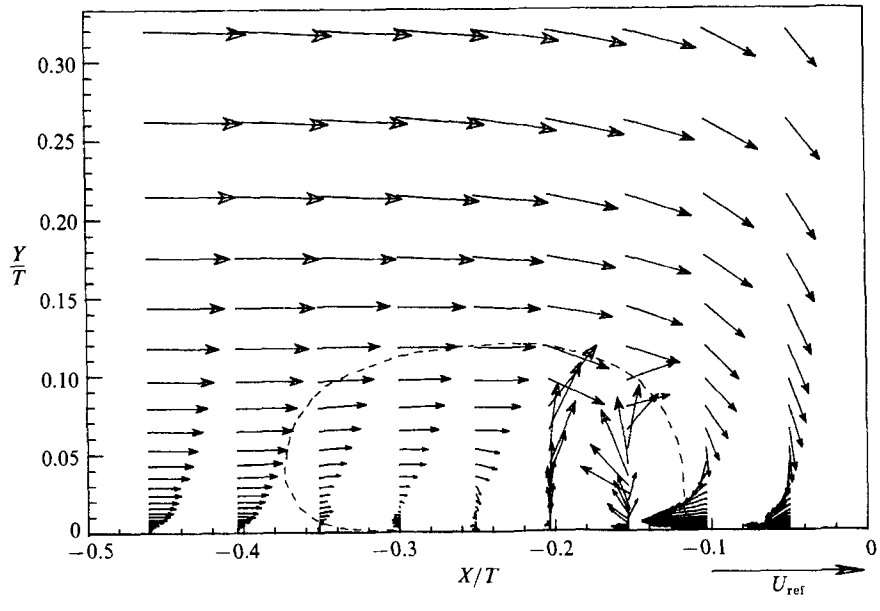

FIGURE 13. Velocity vectors of the zero-flow mode (dotted line shows the extent of the aggregate of the bimodal regions of figure 5).

bimodal histograms result from unsteadiness on the scale of the bimodal region then contours of γ_b represent likely instantaneous limits of the region occupied by the backflow mode. Probable flow patterns at various stages of the large-scale unsteadiness may therefore be constructed by plotting, for each γ_b contour, vectors of the backflow mode downstream and vectors of the zero-flow mode upstream. From

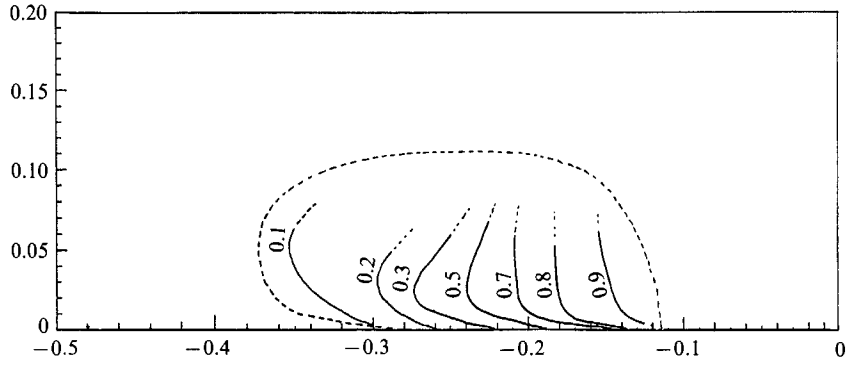

FIGURE 14. Contours of γ_b (the fraction of time for which the backflow mode is present).

these patterns, presented in figure 15, and from those of figures 12 and 13, we propose the following time-dependent flow structure.

For between 20 and 30% of the time (figures 13 and 15*a*) the recirculation region, formed by the reversal of fluid impinging on the wing, is much smaller than on average (figure 5). The backflow associated with this recirculation separates near $X/T = -0.2$ where there are large velocities normal to the wall. (This is where $\overline{v^2}$ reaches its maximum value.) As a result of this separation a weak secondary recirculation is formed upstream, centred near $X/T = 0.3$. For the other 70–80% of the time the fluid reversed by the wing does not reseparate in this fashion. Instead it continues upstream as a 'jet' of near-wall backflow (figure 15*b*, *c*). Some of the time part of this fluid does lift away from the wall and recirculate (figures 15*d*, *e* and 12), but over a much larger region than on average.

An intermittent reversed jet like that proposed above has been observed by Falco in the flow of a turbulent boundary layer past a circular cylinder mounted normal to a wall. Falco's visualization (see plate 165 in Van Dyke 1982), performed in the plane of symmetry upstream, appears to show the jet being formed from irrotational free-stream fluid that has penetrated into the corner between the wing and wall. This suggests a connection between the unsteady flow structure we have proposed and the nature of fluid flowing into the corner region.

Consider a situation in which a body of fluid from a rotational, presumably outer-region, boundary-layer structure arrives in the corner region. (This must happen at some time since our velocity measurements show significant Reynolds shear stresses here.) This fluid would have relatively low momentum. It would therefore be particularly susceptible to cross-stream pressure gradients and be lost fairly rapidly from the nose region. During this process its spanwise vorticity would be stretched and concentrated. It is easy then to think of this fluid forming the relatively small recirculation region of figures 13 and 15(*a*). Consider now a situation in which a body of fluid from the free stream arrives in the corner region. Since this fluid would be irrotational and have a greater momentum it seems unlikely that it could be accommodated simply by an increase in the size of this rotational region of recirculation. Perhaps to preserve its irrotationality it must form the reversed 'jet' observed above before loosing its streamwise momentum and moving out of the nose region.

Given this explanation figure 15 implies that fluid arriving in the corner region has a turbulent/non-turbulent intermittency of between 0.2 and 0.3 which, following the

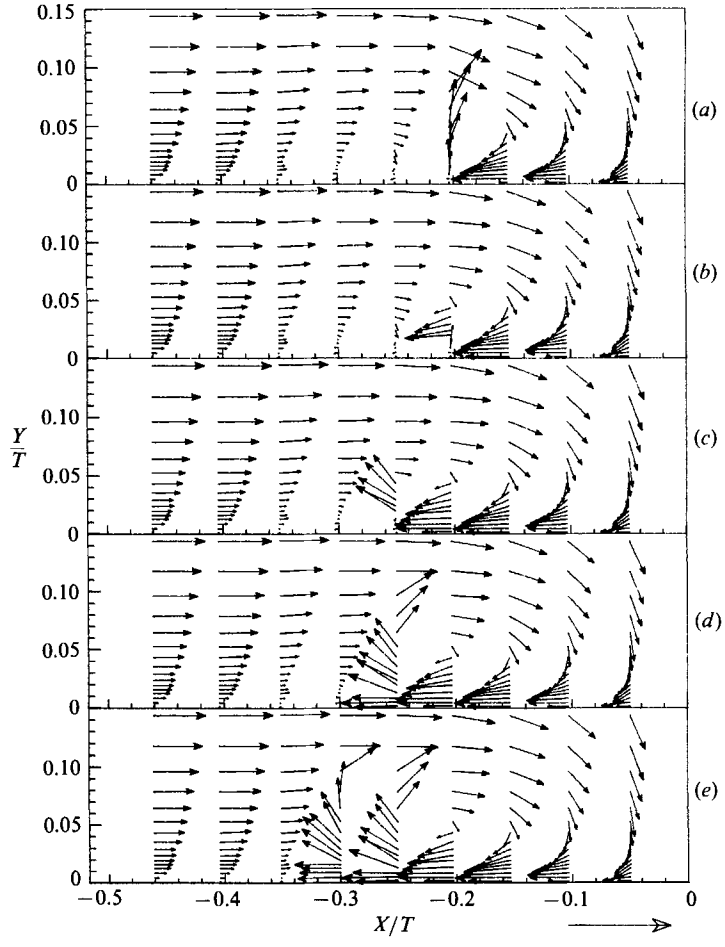

FIGURE 15. Velocity vectors of the zero-flow mode and the backflow mode combined for (*a*) $\gamma_b = 0.8$, (*b*) $\gamma_b = 0.7$, (*c*) $\gamma_b = 0.4$, (*d*) $\gamma_b = 0.2$, (*e*) $\gamma_b = 0.1$.

results of Fiedler & Head (1966), we would expect between $Y/\delta = 0.8$ and 1.05 in the approaching boundary layer.

The mechanism we have proposed could occur in front of any forward-facing part of the wing nose and indeed, in recent measurements (Devenport & Simpson 1988), we have observed bimodal histograms of velocity fluctuations as far downstream as the maximum thickness of the wing. However, since the turbulent/non-turbulent interface must be strongly three-dimensional in the nose region we would not expect the near-wall structure we have described have an instantaneous spanwise extent greater than, say, the boundary-layer thickness.

As far as the authors are aware no previous published work has conclusively demonstrated the presence of bimodal velocity histograms in a wing–body junction flow. Tree (1986) presented time-averaged spectra of the photomultiplier signal of a laser anemometer recorded in the vicinity of the mean junction vortex upstream of a circular-nosed wing. A few of these appear bimodal. However, such spectra are not truly equivalent to velocity p.d.f.s. Tree did not comment on the unusual form of his results.

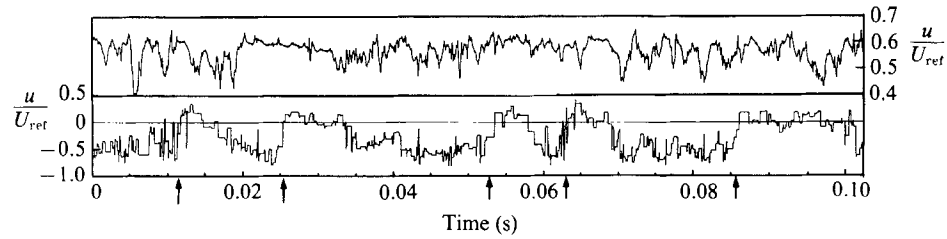

FIGURE 16. Simultaneous velocity records at $X/T = -0.2$. Upper trace, hot wire at $Y/T = 0.4$. Lower trace. LDV at $Y/T = 0.007$. Transitions between the backflow and zero-flow modes marked by the arrows.

In recent, as yet unpublished, work we have observed bimodal histograms in the plane of symmetry in front of: the present wing with a 50% thinner approach boundary layer; the present wing with flow-control devices attached to the nose; and the Rankine half-body of Moore & Furlini (1984). This phenomenon is therefore not peculiar to the present configuration or boundary layer.

3.4. *Short-time cross-correlations*

An experiment was devised to examine directly some of the time-dependent behaviour of the flow and to test the proposed relationship between the structure of the outer part of the approach boundary layer and large-scale fluid motions associated with the bimodal histograms.

A single hot-wire probe was positioned in the plane of symmetry at $X/T = -0.2$, $Y/T = 0.4$ (93% of the local boundary-layer thickness) in the outer intermittent region. The measurement volume of the laser anemometer was simultaneously traversed at this same X-location to a number of positions within the region of bimodal flow ($Y/T = 0.007$ to 0.029, see figures 11 and 15 to visualize these positions). Here the LDV was expected to detect the sudden changes in velocity implied by the bimodal U-p.d.f.s and (given our explanation) associated with the formation and disappearance of an intermittent reversed jet. By using only the U-sensitive beams of the U, W optical system, a sufficiently high signal-to-noise ratio was obtained to allow us to use a TSI counter (model 1980) to process the signal from the photomultiplier tube. Though the counter settings were adjusted to minimize the number of false velocity measurements produced by noise, data rates in excess of 10000 velocity samples per second were not difficult to obtain. It should be noted that the comparison circuits of the counter (which help distinguish between Doppler bursts and noise) have since been found to have a fault which would have caused a proportion of valid Doppler bursts to be rejected as noise. However, it is not thought that this had any significant effect on any of the results presented here. The analogue voltage output of the counter and the signal from the hot wire were recorded simultaneously at a sampling rate of 33 kHz using a Data Precision Data 6000 analogue-to-digital converter. 18.4 s of data were taken for each position of the LDV.

Simultaneous velocity records measured with the hot wire and LDV, with the latter located at $Y/T = 0.007$, are shown in figure 16. (This was the closest the U, W optical system could be brought to the wall because of the effects of flare.) The hot-wire signal has the expected intermittent character although there are fewer periods of relative inactivity, indicating the passage of non-turbulent fluid, than might normally be expected at this position in a boundary layer. This presumably is a consequence of the extreme distortion of the boundary layer that must occur this

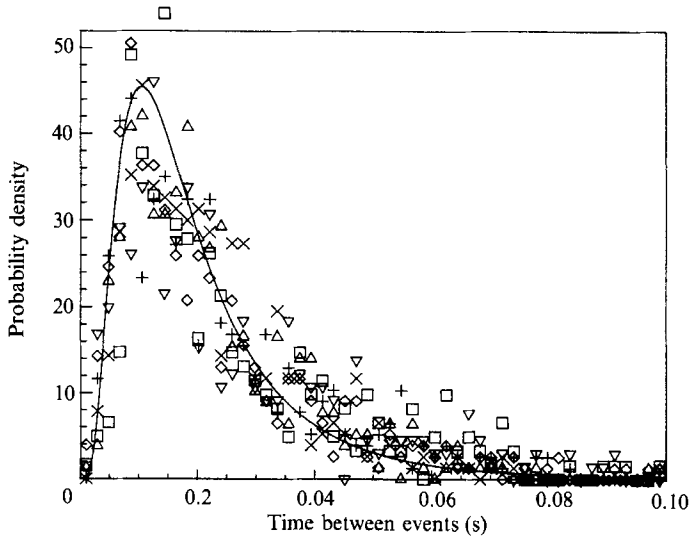

FIGURE 17. Histograms of the time between events (transitions between back- and zero-flow modes) at $X/T = -0.2$: □, $Y/T = 0.007$; ×, 0.009; △, 0.012; +, 0.016; ▽, 0.022; ◇, 0.029. Solid line represents a log-normal distribution.

close to the wing. The LDV signal has periods in which the velocity remains large and negative and periods in which the velocity is much smaller and fluctuates around zero. These two states correspond respectively to the backflow and zero-flow modes presumed from the two peaks in the bimodal velocity histograms.

An examination of figure 16 and the rest of the time records reveals that the transition between the backflow and zero-flow modes in the LDV signal is almost invariably rapid (the transition back is sometimes rapid and sometimes gradual). This transition (from back- to zero-flow mode) is both easily distinguished from the rest of the velocity trace and well defined in time. We were therefore able to identify and obtain the temporal locations of all such events in the LDV signal simply by eye, there being about 580 in the 15.3 s of data analysed for each location. That the number of events is approximately independent of Y is at first surprising. In this region the velocity p.d.f.s (figure 11) show, with increasing Y, a reduction in the relative magnitude of the peak associated with the zero-flow mode, implying a reduction in the proportion of time that this mode is present. It seems then that this must be achieved not by a reduction in the number of periods of zero-flow mode but by a reduction in their length.

Histograms of the time between events for the various LDV positions were constructed and are plotted in figure 17. Consistent with the above conclusion there is little change in these histograms with Y. They all have approximately the same log-normal form showing a large variation in the time between events. This irregularity of the unsteadiness suggests that it was a truly turbulent phenomenon and not associated with any artificial excitation of the flow, such as vibration of the model (which was firmly bolted to a steel mount) or blower noise (which was minimal). The most common time between events in figure 17 is about 0.011 s and the mean time between events is about 0.026 s. The frequencies corresponding to these periods are 91 Hz, or $0.12U_{\mathrm{ref}}/\delta_{99.5}$, and 38 Hz, or $0.05U_{\mathrm{ref}}/\delta_{99.5}$, respectively, where $\delta_{99.5}$ is the thickness of the approach boundary layer at $X = -2.15T$. These are close to or within the range of non-dimensional frequencies found by Rood (1984) and

Hasan *et al.* (1985) to be important near the nose of similar appendage–body junctions. They are, however, significantly smaller than the most energetic frequency of velocity fluctuations in the outer region of the boundary layer, obtained from the signal of the hot-wire probe at $Y/T = 0.4$. This frequency, $0.25U_{\mathrm{ref}}/\delta_{99.5}$, was taken as the position of the peak in the first moment of the hot-wire velocity spectrum, which Strickland & Simpson (1975) show to be mathematically identical to the most energetic frequency of velocity fluctuations, as would be obtained through short-time autocorrelations.

The difference in frequency does not imply that the instantaneous characteristics of the junction structure are unrelated to the structure of the outer part of the boundary layer. Indeed we might expect this difference since only a fraction of the boundary-layer fluid can recirculate in the corner between the wing and wall, the rest being carried out of the nose region in the spanwise direction. If there is a relationship then a correlation should exist between some of the velocity fluctuations recorded by the hot-wire in the outer part of the boundary layer and the transition between the backflow and zero-flow modes seen in the LDV signal. This possibility was investigated using short-time correlations since long-time correlations and coherence functions revealed nothing of significance.

Time-delay correlations between a kernel of the LDV signal 0.018 s long, centred on each sudden change in velocity between the backflow and zero-flow modes (see figure 16), and the hot-wire signal were calculated. The resulting correlation-coefficient functions were averaged over all such events for each position of the LDV. Note that to reduce computation times only every fourth point was correlated and the LDV signal was treated as though it were continuous. Average short-time correlation-coefficient functions (uncertainty about ± 0.02) are plotted in figure 18. As with the histograms of figure 17 these do not vary significantly with Y, supporting our assumption that the bimodal histograms are associated with large-scale structure. All the curves show a significant negative correlation that reaches a peak at a time delay of about -3 ms. This indicates that the change from a high-velocity backflow to a flow of near zero velocity at the LDV locations (which would coincide with the disappearance of the intermittent reversed jet) is preceded by a drop in the velocity measured by the hot wire near the edge of the boundary layer (which would normally accompany the arrival of a body of low-momentum turbulent fluid). While this result does not conclusively demonstrate that the bimodal unsteadiness depends on the turbulent/non-turbulent origin of fluid arriving in the corner region it is what would be expected given the mechanisms we have proposed.

An order-of-magnitude calculation, assuming a convection velocity of $0.29U_{\mathrm{ref}}$ (half the local free stream) and guessing the distance travelled by fluid in recirculating between the hot wire and LDV positions as $0.5T$, yields a delay time of 4.5 ms. This difference, if significant, may be accounted for by the fact that at 93% of the boundary-layer thickness the hot wire might only detect the top part of a boundary-layer structure, the bottom of which travels a shorter distance before arriving in the corner region.

The curves of figure 18 do show a significant correlation at zero time delay and small positive time delays. While this could be due to distortion of the boundary-layer structure in the nose region we suspect that it is a result of the finite length of the correlation kernel. Consider for example the short-time correlation between two simultaneous step functions which does not fall to zero until the time delay exceeds half the kernel size. Calculations were performed using shorter kernels but the resulting estimates of average correlation coefficient were too uncertain to be useful.

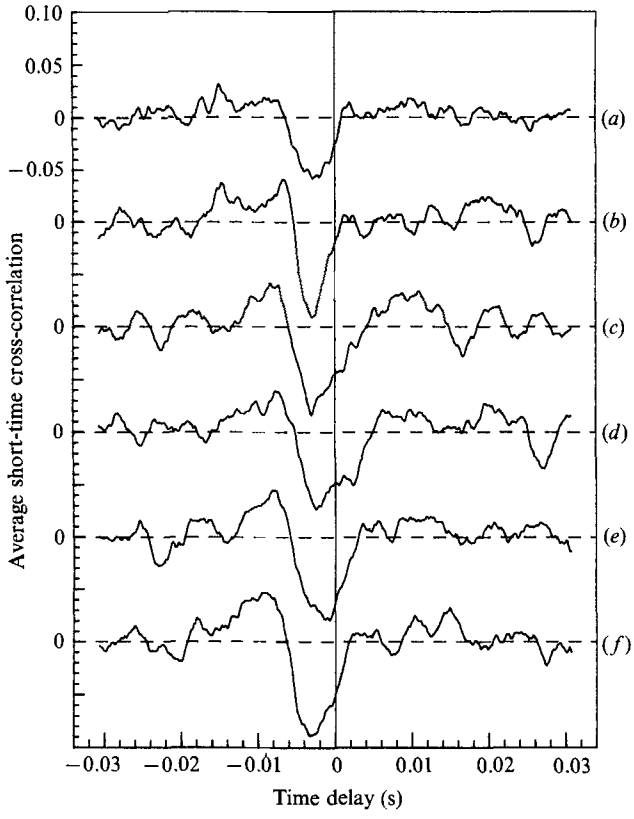

FIGURE 18. Average short-time cross-correlations between velocity signals measured with the hot wire at $Y/T = 0.4$ and with the LDV at (*a*) $Y/T = 0.029$, (*b*) 0.022, (*c*) 0.016, (*d*) 0.012, (*e*) 0.009, (*f*) 0.007.

3.5. *Turbulence kinetic energy balance*

To further reveal the turbulence structure and its effect on the Reynolds-averaged properties of the flow in the plane of symmetry, measurements made using the laser anemometer have been used to estimate the magnitude of some terms in the turbulence kinetic energy equation. This analysis also enables us to examine this flow from the point of view of the computor.

For three-dimensional flows the turbulence kinetic energy equation, written in summation-subscript notation, is

$$0 = -U_l\frac{\partial\overline{q^2}}{\partial x_l} - 2\overline{u_i u_l}\frac{\partial U_i}{\partial x_l} - \frac{\partial\overline{q^2 u_l}}{\partial x_l} - \frac{2}{\rho}\frac{\partial\overline{pu_l}}{\partial x_l} + 2\nu\overline{u_i\frac{\partial^2 u_i}{\partial x_l^2}}, \tag{1}$$

where $\overline{q^2} = \overline{u^2}+\overline{v^2}+\overline{w^2}$ (Townsend 1956). In the plane of symmetry W, $\overline{vw}$, $\overline{uw}$ and $\partial\overline{q^2}/\partial Z$ are zero. These simplifications, after expanding and non-dimensionalizing the equation, give

$$0 = \frac{T}{U_{\text{ref}}^3}\left\{-U\frac{\partial\overline{q^2}}{\partial X} - V\frac{\partial\overline{q^2}}{\partial Y}\right\} + \frac{T}{U_{\text{ref}}^3}\left\{-2\overline{u^2}\frac{\partial U}{\partial X} - 2\overline{v^2}\frac{\partial V}{\partial Y} - 2\overline{w^2}\frac{\partial W}{\partial Z} - 2\overline{uv}\left(\frac{\partial U}{\partial Y}+\frac{\partial V}{\partial X}\right)\right\}$$

$$+\frac{T}{U_{\text{ref}}^3}\left\{-\frac{\partial\overline{u(q^2+2p/\rho)}}{\partial X} - \frac{\partial\overline{v(q^2+2p/\rho)}}{\partial Y} - \frac{\partial\overline{w(q^2+2p/\rho)}}{\partial Z}\right\} - \frac{T}{U_{\text{ref}}^3}\{e\}, \tag{2}$$

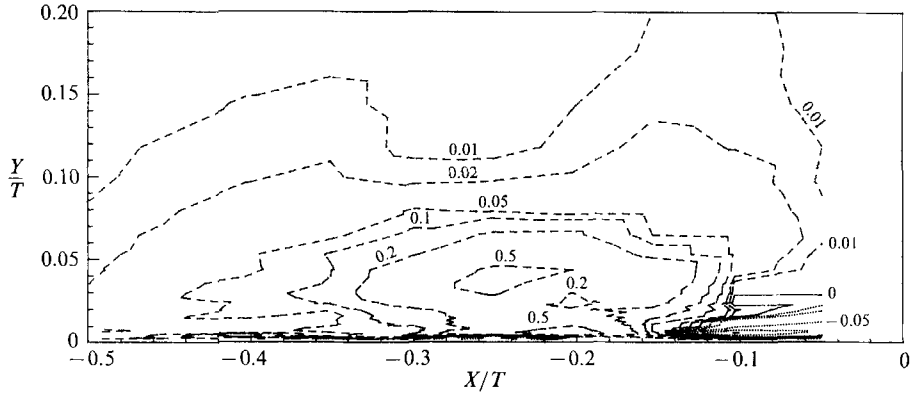

FIGURE 19. Contours of production of turbulence energy normalized on U_{ref}^3/T.

neglecting viscous diffusion. From left to right the bracketed groups of terms represent advection, production, diffusion and dissipation of turbulence energy.

Measurements of U, V, $\overline{u^2}$, $\overline{v^2}$, $\overline{w^2}$ and $-\overline{uv}$ were used to estimate the component terms of the production and advection. To do this Y-differentials were computed by fitting a parabola to each adjacent set of five points by the method of least squares. Gradients with respect to X were computed by fitting a parabola to adjacent sets of three points except at the streamwise limits of the data set where a linear fit was used. $\partial W/\partial Z$ was calculated using the mean continuity equation. Uncertainties for the estimated terms are included in table 1.

Figure 19 shows contours of the total production of turbulence energy in the plane of symmetry. The contours indicate a region of intense positive production between $X/T = -0.14$ and -0.34. This region is approximately coincident with the regions of bimodal flow (figure 5), suggesting that this production is a result of the large-scale unsteadiness proposed above rather than conventional shear-layer mechanisms. The contours also show some negative production in the corner between the wall and the wing leading edge.

Figure 20 compares the component terms of production at several streamwise locations. This figure reveals variations of production in the near-wall region more clearly. As might be expected, most of the production of turbulence energy in the boundary layer at $X/T = -0.65$, upstream of separation, occurs close to the wall and is a consequence of the Reynolds-shear-stress term $-2\overline{uv}\,\partial U/\partial Y$. By $X/T = -0.40$, however, just downstream of separation, peak production has moved away from the wall and is principally a result of the normal-stress term $-2\overline{u^2}\,\partial U/\partial X$. The influence of the junction vortex is apparent in the much increased production at $X/T = -0.30$. Here there are two peaks in the distribution of total production, both in the backflow region. The first (only just discernible in figure 20) is located very close to the wall near $Y/T = 0.004$ and the second, near $Y/T = 0.03$, is within the regions of bimodal flow. The shear- and normal-stress terms, $-2\overline{uv}\,\partial U/\partial Y$ and $-2\overline{u^2}\,\partial U/\partial X$, are both important at this location. Two peaks in the production distribution can also be seen at $X/T = -0.25$ and -0.20 on the upstream side of the mean vortex, though the overall production is much greater at these locations. The inner peak near $Y/T = 0.006$, associated with normal-stress production $-2\overline{u^2}\,\partial U/\partial X$, results from the rapid deceleration of the backflow at these two locations (figure 5) and the high turbulence levels resulting from bimodal flow. The outer peak, located near the mid-height of the

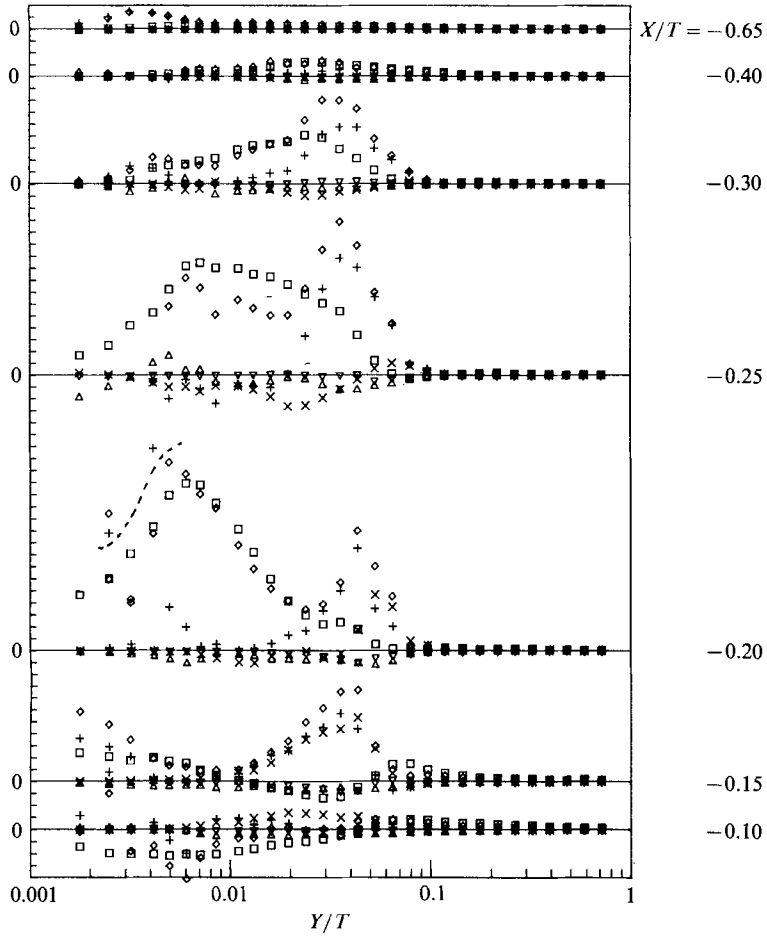

FIGURE 20. Component terms of the turbulence energy production: □, $-2\overline{u^2}\partial U/\partial X$; ×, $-2\overline{v^2}\partial V/\partial Y$; △, $-2\overline{w^2}\partial W/\partial Z$; +, $-2\overline{uv}\partial U/\partial Y$; ▽, $-2\overline{uv}\partial V/\partial X$; ◇, total production. Divisions on vertical axis $0.5U_{\text{ref}}^3/T$.

junction vortex, is principally due to shear-stress production $-2\overline{uv}\partial U/\partial Y$, which is large because of a shear stress augmented by bimodal flow and substantial $\partial U/\partial Y$ associated with the centre of the mean vortex. Small but significant amounts of $-2\overline{v^2}\partial V/\partial Y$ also appear in the vicinity of the outer peak. The large negative production close to the wall at $X/T = -0.25$ is a result of a steep negative velocity gradient $\partial U/\partial Y$ associated with the backflow here, and a positive Reynolds shear stress $-\overline{uv}$ produced by bimodal flow.

On the downstream side of the mean vortex, between $X/T = -0.20$ and -0.10 there is a substantial fall in production. This is partly due to a drop in $-2\overline{u^2}\partial U/\partial X$, which becomes negative at $X/T = -0.10$ because of the acceleration of the mean backflow here. While the contribution to the total production from $-2\overline{uv}\partial U/\partial Y$ is still significant at $X/T = -0.15$ and -0.10, $-2\overline{v^2}\partial V/\partial Y$ is also important because of the substantial wallward flow in this region. Production resulting from $-2\overline{w^2}\partial W/\partial Z$ and $-2\overline{uv}\partial V/\partial X$ seems to be largely insignificant in the plane of symmetry.

Contours of total advection are drawn in figure 21. Component terms are compared in figure 22. Unlike those of production, the contours of advection are not centred on

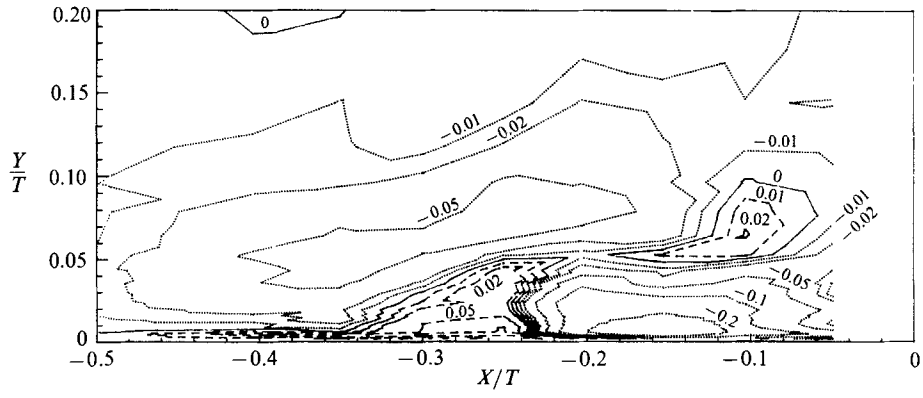

FIGURE 21. Contours of advection of turbulence energy normalized on U_{ref}^3/T.

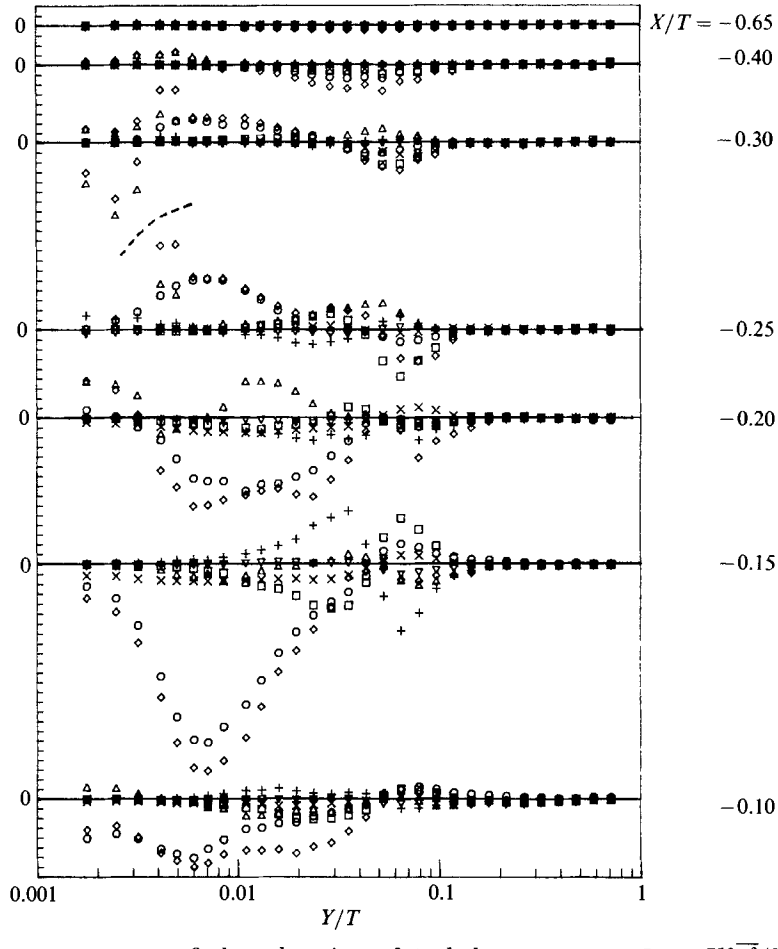

FIGURE 22. Component terms of the advection of turbulence energy: ○, $-U\partial\overline{u^2}/\partial X$; □, $-U\partial\overline{v^2}/\partial X$; ×, $-U\partial\overline{w^2}/\partial X$; △, $-V\partial\overline{u^2}/\partial Y$; +, $-V\partial\overline{v^2}/\partial Y$; ▽, $-V\partial\overline{w^2}/\partial Y$, ◇, total advection. Divisions on vertical axis $0.2U_{\text{ref}}^3/T$.

the region of bimodal flow because the advection does not depend on absolute values of the turbulent stresses. Instead they are mostly concentrated in four regions surrounding the middle of the mean vortex. The first of these, a negative region located to the upper left of the vortex centre, extends upstream into the approach boundary layer. Here advection is extracting energy primarily because of the increase in turbulence energy with distance downstream in the separating boundary layer and over the upstream half of the mean junction vortex. The terms $-U\partial\overline{u^2}/\partial X$, $-U\partial\overline{v^2}/\partial X$ and $-U\partial\overline{w^2}/\partial X$ are most important here.

In the second region, located to the upper right of the vortex centre, advection is mildly positive, adding to the local balance of turbulence energy. Here the mean flow (figure 5), having come over the top of the vortex, is moving back down towards the wall. This fluid is experiencing a loss of $\overline{u^2}$ as it moves downstream but a gain in $\overline{v^2}$ as it approaches the wall. The total advection is therefore a sum of several terms associated with both X- and Y-gradients of turbulence energy.

In the third region, to the lower right of the vortex centre, the advection is large and negative. This region almost exactly encloses the backflow between the wing leading edge and the centre of the mean vortex. Much of this flow may originate from the outer part of the boundary layer and therefore has less turbulence energy than the surrounding fluid. Its movement upstream therefore subtracts from the balance of turbulence energy mostly through the term $-U\partial\overline{u^2}/\partial X$ and, to a lesser extent, through the terms $-U\partial\overline{v^2}/\partial X$ and $-U\partial\overline{w^2}/\partial X$.

The final (positive) region, to the lower left of the vortex centre, extends into the near-wall region of the approach boundary layer. The gain of turbulence energy in this near-wall region (where the mean flow is still mostly in the downstream direction) is principally due to $-V\partial\overline{u^2}/\partial Y$. This is important because of the movement away from the wall of the peak in $\overline{u^2}$ here (see figure 9*b*) to a region where V is significant. Near the vortex centre the positive advection is due mostly to $-U\partial\overline{u^2}/\partial X$ because of significant backflow velocities and the increase in $\overline{u^2}$ with X. Contributions to advection from $-V\partial\overline{w^2}/\partial Y$ do not appear to be important in the plane of symmetry.

The diffusion and dissipation terms of the turbulence kinetic energy equation could not be estimated directly. However, contours of their sum, plotted in figure 23, have been drawn from the negative of the sum of the production and advection terms. In this plot the contribution from dissipation must always be negative. Figure 23 therefore shows a strong diffusion of turbulence energy into fluid in the corner region between the wall and leading edge of the wing. This is consistent with the idea that at least some of this is non-turbulent fluid brought here from the outer region of the boundary layer. In the bimodal region figure 23 shows negative contours. We would argue that these are mostly due to diffusion. This is because our analyses of the bimodal region imply the presence of instantaneous structures large in comparison to the probable scale of energy-dissipating eddies. It would therefore be surprising if these structures were associated with an increase in dissipation sufficient to account for these large negative values.

As a matter of course we have examined the behaviour of the eddy viscosity, mixing length and Prandtl–Kolmogorov lengthscale in this flow. Upstream of separation these quantities vary in ways consistent with the analogy of a two-dimensional boundary layer in an adverse pressure gradient. However, downstream in the vicinity of the junction vortex, these parameters are probably of little use, their variations being greater than those of the turbulence stresses they are used to model. While the failure of these simple concepts is hardly surprising we anticipate

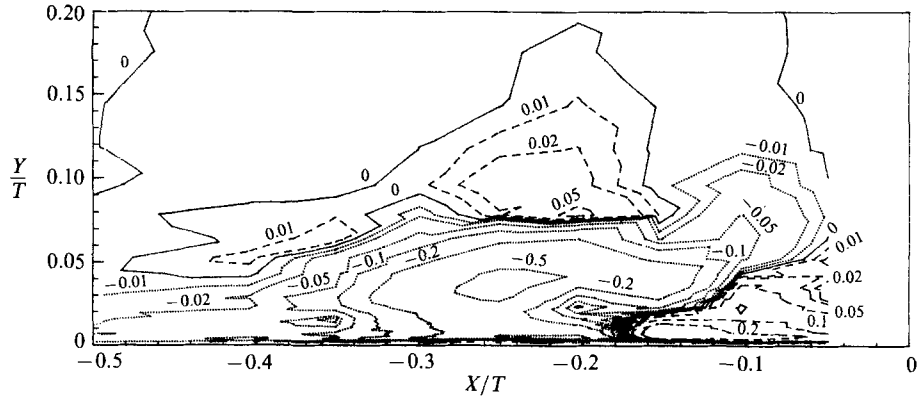

FIGURE 23. Contours of diffusion + dissipation of turbulence energy normalized on U_{ref}^3/T.

that many other, more sophisticated, turbulence models will also perform poorly. This is because such models, which either imply or directly specify the form of the velocity p.d.f., are unlikely to be able to predict the variations of turbulence stresses associated with the bimodal velocity histograms. One possible approach may be to compute the flow patterns of the zero- and backflow modes separately. However, it is not clear from the present data how two such solutions could be combined *a priori*.

4. Conclusions

The behaviour of a turbulent boundary layer on a flat surface as it encounters the nose of a wing projecting normal to that surface has been investigated. Measurements made using a three-component laser anemometer in the plane of symmetry upstream of the wing for the first time reveal in detail the turbulence structure of this flow.

The adverse pressure gradient in the plane of symmetry causes the boundary layer approaching the wing to separate. Upstream of separation and in the vicinity of the separation point mean-velocity and turbulence-stress profiles appear like those of a two-dimensional boundary layer separating in an adverse pressure gradient. This similarity is only qualitative, though, the growth of the boundary layer and movement away from the wall of the peak turbulence stresses being inhibited by the local removal of fluid from the boundary layer in the spanwise direction. For a short distance downstream of separation, mean backflow is present only in a thin region adjacent to the wall. Flow reversals are common here and velocity gradients at the wall are small. This backflow may be generated locally by the turbulent structures of the boundary layer as they decelerate in the adverse pressure gradient. This zone extends downstream to where a line of locally low wall shear stress crosses the plane of symmetry. This line, observed in the oil-flow visualization, extends around the nose of the wing downstream of the primary separation line. In the vicinity of the line of low shear, the flow moves away from the wall to accommodate the presence of the time-mean junction vortex. This structure, an intense approximately elliptical recirculation, is centred about one-tenth of the undisturbed boundary-layer thickness from the wall. In its vicinity the turbulent stresses become very large, reaching maximum values much greater than those normally observed in turbulent boundary layers. $\overline{v^2}$ and $-\overline{uv}$ reach their peak values in an area of high mean-velocity gradient close to the centre of the mean vortex. The maximum of $\overline{u^2}$ occurs much closer to the

wall in the region of intense backflow. The large stresses are associated with bimodal (double-peaked) probability-density functions of U and V that occur over a region encompassing most of the mean vortex. The velocity variation with time that produces these p.d.f.s is bistable and switches between two states, one of large negative U (the backflow mode) and one of near-zero U (the zero-flow mode), at most locations.

The two peaks of each bimodal p.d.f. may be separated in an approximate way to yield estimates of the average velocity vectors associated with each mode and an estimate of the proportion of time for which the backflow mode is present, γ_b. Assuming the two modes are generated by some unstable large-scale structure, contours of γ_b represent likely instantaneous limits of the region occupied by the backflow mode. Thus probable flow patterns at various stages of the large-scale unsteadiness may be constructed from a combination of the velocity fields associated with the zero- and backflow modes. These patterns show that for between 20 and 30 % of the time the region of recirculation, formed by the reversal of fluid impinging on the wing, is much smaller than on average. The backflow associated with this recirculation separates and a weak secondary recirculation is formed upstream. For the rest of the time the fluid reversed by the wing does not separate in this fashion but continues upstream as a jet of near-wall backflow. (An intermittent jet of this type is apparent in the flow visualization of Falco, see Van Dyke 1982.)

Mean-velocity measurements and Falco's visualization suggest that at least some of the fluid reversed by the wing comes from the outer intermittent part of the boundary layer. We therefore propose that the presence or absence of the reversed jet depends on whether this fluid originates from a low-momentum boundary-layer structure or from the irrotational free stream. Short-time cross-correlations between velocity signals measured in the outer part of the boundary layer and in the backflow region tend to confirm this hypothesis. However, the frequency of large-scale fluctuations in the backflow, $0.05U_{\mathrm{ref}}/\delta_{99.5}$ (derived from the mean period between transitions from the backflow to the zero-flow modes), is substantially lower than the typical passage frequency of structures in the outer part of the boundary layer, $0.25U_{\mathrm{ref}}/\delta_{99.5}$. Thus only a fraction of these structures can affect the recirculation, the rest presumably being carried away in the spanwise direction.

The various components of the production and advection terms of the turbulence kinetic energy equations were estimated from the velocity measurements. This analysis shows that the region of bimodal flow surrounding the time-mean junction vortex is one of intense turbulence production. We do not see this production as resulting from conventional mechanisms but from the large-scale unsteadiness of the flow described above. The advection in this vicinity is concentrated in several positive and negative regions surrounding the centre of the time-mean vortex. There is a strong diffusion of turbulence energy into the backflow region in the corner between the wing and wall. With the possible exceptions of $-2\overline{w^2}\,\partial W/\partial Z$, $-2\overline{uv}\,\partial V/\partial X$ and $-V\,\partial\overline{w^2}/\partial Y$ all the component terms of the production and advection are important in the plane of symmetry.

The bimodal histograms seem to be a very important feature of the turbulence structure of this flow. Unfortunately this feature is likely to make the development of successful prediction methods much harder, especially those that imply or directly specify the form of the velocity probability density function.

A full data report, including the measurements presented in this paper, is available (Devenport & Simpson 1987). These data are also available on magnetic media.

The authors would like to thank Mr Semih Olcmen for the potential flow calculation and for his help in taking some of the above measurements. This work was sponsored by NAVSEA through NSWC contract N60921-83-G-A165-B02.

REFERENCES

ABID, R. & SCHMITT, R. 1986 Experimental study of a turbulent horseshoe vortex using a three-component laser velocimeter. *AIAA*-86-1069, *AIAA/ASME 4th Fluid Mechanics, Plasma Dynamics and Lasers Conference, Georgia.*

AHN, S. 1986 Unsteady features of turbulent boundary layers. M.S. thesis, Virginia Polytechnic Institute and State University.

BAKER, C. J. 1980 The turbulent horseshoe vortex. *J. Wind Engng Indust. Aerodyn.* **6**, 9–23.

BELIK, L. 1973 The secondary flow about circular cylinders mounted normal to a flat plate. *Aero Q.* **24**, 47–54.

DECHOW, R. & FELSCH, K. O. 1977 Measurements of the mean velocity and of the Reynolds stress tensor in a three-dimensional turbulent boundary layer induced by a cylinder standing on a flat wall. In *Turbulent Shear Flows Symp., Pennsylvania State University*, pp. 9.11–9.20.

DEVENPORT, W. J. & SIMPSON, R. L. 1986 Some time-dependent features of turbulent appendage–body juncture flows. In *16th Symposium on Naval Hydrodynamics, July 14–18, Berkeley, CA* (ed. W. C. Webster), pp. 312–335. National Academic Press.

DEVENPORT, W. J. & SIMPSON, R. L. 1987 An experimental investigation of the flow past an idealized wing–body junction: data report. Dept. of Aerospace and Ocean Engineering, Virginia Polytechnic Institute and State University.

DEVENPORT, W. J. & SIMPSON, R. L. 1988 LDV measurements in the flow past a wing–body junction. *Fourth Intl Symp. on Applications of Laser Anemometry to Fluid Mechanics, Lisbon, Portugal.*

DEVENPORT, W. J. & SIMPSON, R. L. 1989 Time-dependent structure in wing–body junction flows. *Turbulent Shear Flows 6.* Springer.

DICKINSON, S. C. 1986 An experimental investigation of appendage – flat plate junction flow. Vol. 1, Description. *David Taylor Naval Ship Research and Development Center Rep.* 86/051.

DURST, F., MELLING, A. & WHITELAW, J. H. 1981 *Principles and Practice of Laser Dopper Anemometry*, Academic.

ECHOLS, W. H. & YOUNG, J. A. 1963 Studies of portable air-operated aerosol generators. *NRL Rep.* 5929.

FIEDLER, H. & HEAD, M. R. 1966 Intermittency measurements in the turbulent boundary layer. *J. Fluid Mech.* **25**, 719–735.

HARSH, M. D. 1985 Experimental investigation of a turbulent junction vortex. Ph.D. dissertation, Virginia Polytechnic Institute and State University.

HASAN, M. A. Z., CASARELLA, M. J. & ROOD, E. P. 1985 An experimental study of the flow and wall-pressure field around a wing–body junction. *Shear Flow–Structure Interaction Phenomena* (ed. A. Akay & M. Reischman), ASME NCA-1, pp. 89–95.

KUBENDRAN, L. R., MCMAHON, J. & HUBBART, J. E. 1986 Turbulent flow around a wing–fuselage type juncture. *AIAA J.* **24**, 1447–1452.

MCMAHON, H., HUBBART, J. & KUBENDRAN, L. R. 1983 Mean velocities and Reynolds stresses upstream of a simulated wing–fuselage juncture. *NASA CR* 3695.

MEHTA, R. D. 1984 Effect of wing nose shape on the flow in a wing/body junction. *Aeronaut. J.* **88**, 456–460.

MOORE, J. & FURLINI, T. J. 1984 A horseshoe vortex in a duct. *Trans. ASME J.: J. Engng Gas Turbines and Power* **106**, 668–676.

ROOD, E. P. 1984 Experimental investigation of the turbulent large scale temporal flow in the wing–body junction. Ph.D. dissertation, The Catholic University of America.

SANDBORN, V. A. & SLOGAR, R. J. 1955 Study of the momentum distribution of turbulent boundary layers in adverse pressure gradients. *NACA Tech. Note* 3264.

SCHLICHTING, H. 1968 *Boundary-Layer Theory*, 6th edn, pp. 511–512. McGraw-Hill.

SCHUBAUER, G. F. & KLEBANOFF, P. S. 1950 Investigation of separation of the turbulent boundary layer. *NACA Tech. Note* 2133.

SHABAKA, I. M. M. A. & BRADSHAW, P. 1981 Turbulent flow measurements in an idealized wing–body junction. *AIAA J.* **19**, 131–132.

SHILOH, K., SHIVAPRASAD, B. J. & SIMPSON, R. L. 1981 The structure of a separating turbulent boundary layer. Part 3. Transverse velocity measurements. *J. Fluid Mech.* **113**, 75–90.

SIMPSON, R. L. & BARR, P. W. 1974 Velocity measurements in a separating turbulent boundary layer using sampling spectrum analysis. *Proc. Second Intl Workshop on Laser Velocimetry*, II (ed. W. H. Stevenson & H. D. Thompson), pp. 15–43. Hemisphere.

SIMPSON, R. L. & BARR, P. W. 1975 Laser Doppler velocimeter signal processing using sampling spectrum analysis. *Rev. Sci. Instrum.* **46**, 835–837.

SIMPSON, R. L. & CHEW, Y.-T. 1979 Measurements in steady and unsteady separated turbulent boundary layers. *Laser Velocimetry and Particle Sizing* (ed. H. D. Thompson & W. H. Stevenson), pp. 179–196. Hemisphere.

SIMPSON, R. L., CHEW, Y.-T. & SHIVAPRASAD, B. G. 1980 Measurements of a separating turbulent boundary layer. *Southern Methodist University Tech. Rep.* SMU-4-PU.

SIMPSON, R. L., CHEW, Y.-T. & SHIVAPRASAD, B. G. 1981 The structure of a separating boundary layer. Part 1. Mean flow and Reynolds stresses. *J. Fluid Mech.* **113**, 23–51.

STRICKLAND, J. H. & SIMPSON, R. L. 1975 Bursting frequencies obtained from wall shear-stress fluctuations in a turbulent boundary layer. *Phys. Fluids* **18**, 306–308.

TOWNSEND, A. A. 1956 *The Structure of Turbulent Shear Flow*, p. 26. Cambridge University Press.

TREE, I. 1986 Laser-Doppler velocimeter measurements in a turbulent junction vortex. Ph.D. dissertation, Virginia Polytechnic Institute and State University.

VAN DYKE, M. 1982 *An Album of Fluid Motion.* Stanford: Parabolic.